

Original Article

Cite this article: Chen C-J and Zhang S-H (2023) Sources and oxidation state of the Permian arc magmatic rocks of SW Jilin Province in the eastern Central Asian Orogenic Belt: evidence from Li, Hf isotopes and oxygen fugacity. *Geological Magazine* **160**: 127–145. <https://doi.org/10.1017/S0016756822000711>

Received: 4 February 2022

Revised: 21 June 2022

Accepted: 22 June 2022

First published online: 27 September 2022



Keywords:

zircon U–Pb geochronology; granitoids; continental-arc magmatic rocks; lithium isotopes; oxygen fugacity; Liaoyuan Accretionary Belt; Central Asian Orogenic Belt (CAOB)

Author for correspondence:

Chang-Jian Chen,
Email: changjian_chen@126.com

Sources and oxidation state of the Permian arc magmatic rocks of SW Jilin Province in the eastern Central Asian Orogenic Belt: evidence from Li, Hf isotopes and oxygen fugacity

Chang-Jian Chen^{1,2,3}  and Shuan-Hong Zhang¹ 

¹Institute of Geomechanics, Chinese Academy of Geological Sciences, MNR Key Laboratory of Paleomagnetism and Tectonic Reconstruction, Beijing 100081, China; ²Gemological Institute, School of Earth Sciences, Guilin University of Technology, Guilin 541004, China and ³Guangxi Key Laboratory of Hidden Metallic Ore Deposits Exploration, School of Earth Sciences, Guilin University of Technology, Guilin 541004, China

Abstract

The late Palaeozoic continental-arc magmatic rocks in the Gongzhuling area are located in the Liaoyuan Accretionary Belt. Here we present new zircon U–Pb ages, whole-rock major- and trace-element compositions, Li and zircon Hf isotopic compositions and oxygen fugacity of these rocks with an aim to constrain the lithium isotopic composition of the source region and origin of the magmas. These rocks were formed during 269–258 Ma in middle–late Permian time. The dioritic rocks were formed through mixing processes, with the mafic melts originating from a metasomatized mantle wedge and the felsic melts from the lower crust of a Neoproterozoic arc. The mantle wedge has been metasomatized by Li-rich fluids derived from subducted oceanic crust, as indicated by the $\delta^7\text{Li}$ values of +0.4 ‰ to +3.5 ‰ and positive $\epsilon_{\text{Hf}}(t)$ values (+0.7 to +13.1). Redox-sensitive Ce in the zircons indicates the $f\text{O}_2$ of the magmas to be low to intermediate (FMQ–2.2 to FMQ+2.6; FMQ is the fayalite–magnetite–quartz redox buffer), precluding large-scale porphyry Cu–Mo mineralization. The middle–late Permian magmatic rocks represent the terminal magmatic record of the subduction of the Palaeo-Asian oceanic crust, meaning that the final closure of the Palaeo-Asian Ocean in the eastern Central Asian Orogenic Belt occurred at the end of the Permian Period. Recent identification of Mesoproterozoic (*c.* 1400 Ma) granites suggests some Palaeoproterozoic crustal fragments still exist in the Liaoyuan Accretionary Belt, but only in a small amount; therefore, it is concluded that the crustal growth of the Liaoyuan Accretionary Belt occurred mainly during the Neoproterozoic period.

1. Introduction

The study area in NE China is in the eastern Central Asian Orogenic Belt (CAOB) and the eastern part of the northern margin of the North China Block (Fig. 1a, b; Wu *et al.* 2011; Zhou & Wilde, 2013; Liu *et al.* 2017). The CAOB is composed of several convergent plate margins and has undergone multi-stage accretionary processes related to subduction of the Palaeo-Asian oceanic plate during Palaeozoic time and subduction of the Palaeo-Pacific oceanic plate during Mesozoic time (Wu *et al.* 2011; Wilde, 2015). There has long been a controversy about the location and timing of the final closure of the Palaeo-Asian Ocean in NE China (Xu *et al.* 2013; Wang *et al.* 2015b), and whether subduction occurred unidirectionally towards the south (Jian *et al.* 2010; Cao *et al.* 2013) or bidirectionally (Xiao *et al.* 2003; Eizenhöfer *et al.* 2014; Yuan *et al.* 2016). There are several main perspectives about the timing of the final closure of the Palaeo-Asian Ocean in NE China: the Middle Devonian (Xu *et al.* 2015), the early–middle Permian (Feng *et al.* 2010), the Early Triassic (Cao *et al.* 2013), the Late Triassic (Xin *et al.* 2011), the middle Mesozoic (Nozaka & Liu, 2002) or the late Permian – Early Triassic (Xiao *et al.* 2009; Xu *et al.* 2013). Therefore, NE China is an ideal area to study these complex arc–continent collisions and the different source regions involved in the generation of the arc magmatism.

Lithium (Li) isotopes are strongly fractionated during low-temperature geological processes, and they can therefore be useful tracers in relatively low-temperature geological environments, including seafloor alteration (Chan *et al.* 2002) and the weathering of continental crust (Rudnick *et al.* 2004; Penniston-Dorland *et al.* 2012; Sauzéat *et al.* 2015). In the circulation of crustal and mantle material in a subduction zone, the relative mass difference of up to 16 % of Li isotopes makes them ideal tracers for studying various geological processes in the subduction zone (Wang *et al.* 2015a). However, almost no effective fractionation of Li isotopes occurs during magmatic processes above 900 °C, which means they can be used to trace magma source regions (Tomascak *et al.* 1999; Teng *et al.* 2006; Marks *et al.* 2007). The weathered continental upper

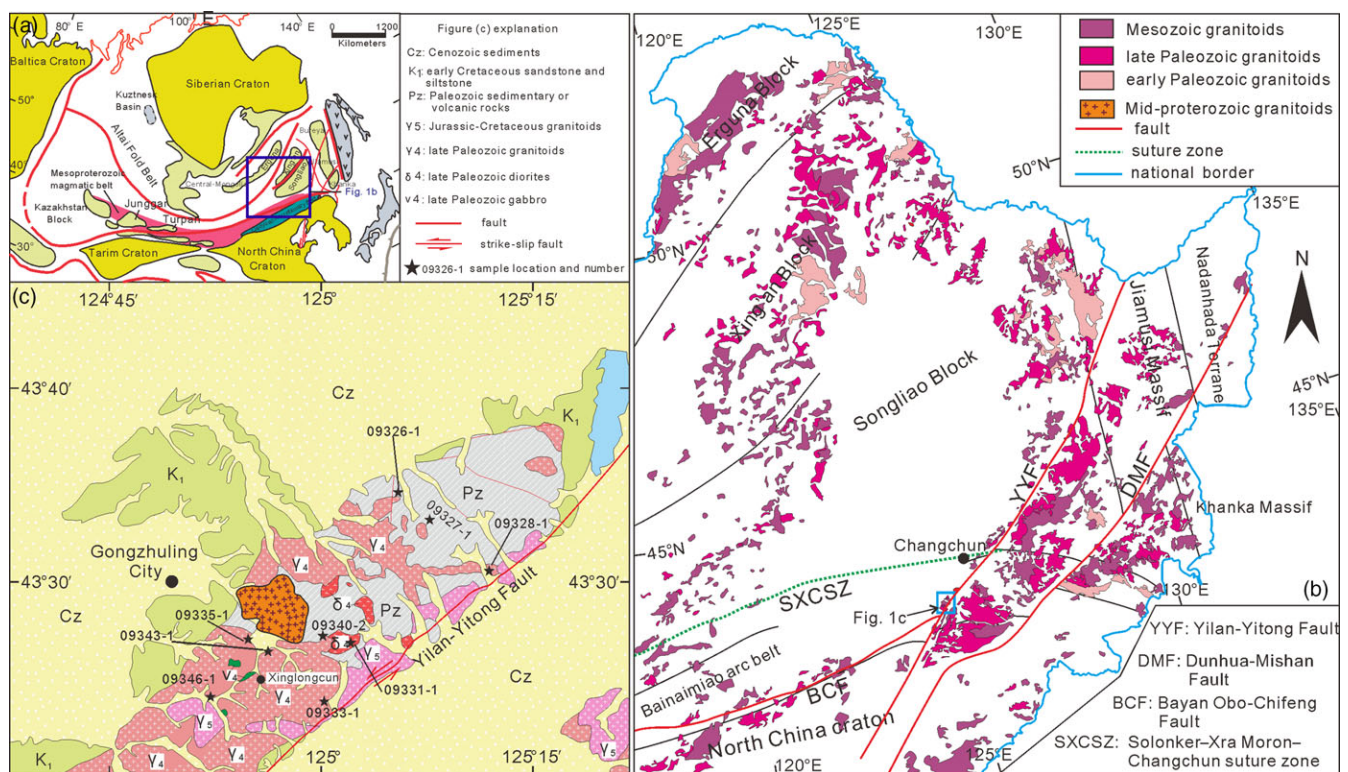


Fig. 1. (Colour online) Overview of the study area. (a) Simplified geological map showing the location of NE China, modified after Zhang *et al.* (2004). (b) Distribution of granitoids and tectonic units of NE China, modified after Wu *et al.* (2007), Zhang *et al.* (2014) and Wang *et al.* (2017). (c) Distribution of granitoids and sampling locations in the Gongzhuling area, SW Jilin Province, NE China.

crust has light $\delta^7\text{Li}$ values ($\delta^7\text{Li} = -5.0\text{‰}$ to 5.0‰ ; Teng *et al.* 2004; Sauz at *et al.* 2015), whereas the lower crust shows large variations in $\delta^7\text{Li}$ values ($\delta^7\text{Li} = -14.0\text{‰}$ to 14.3‰ ; Teng *et al.* 2008). However, the reasons for the heterogeneity of the $\delta^7\text{Li}$ values in the lower continental crust are still debated, and possible factors include mantle source, upper-crust assimilation, isotopic diffusion or metamorphic dehydration (Teng *et al.* 2009; Rudnick & Gao, 2014). It has been suggested that juvenile lower crust and the underlying mantle source region should have uniform Li isotopic compositions (Tomascek *et al.* 1999; Teng *et al.* 2007). Kinetic isotopic fractionation, involving the different diffusion rates of ^6Li and ^7Li , is the commonly given reason for the highly heterogeneous $\delta^7\text{Li}$ values observed in the lower crust (Teng *et al.* 2008; Qiu *et al.* 2011). However, we note that a reasonable interpretation of the geological processes involving the Li isotopes of magmatic rocks has been hampered by inadequately integrating the Li isotopic data with petrological and geochemical data (Parkinson *et al.* 2007; Krienitz *et al.* 2012). Such an integrated approach is essential to relate the combined petrological, geochemical and isotopic data to distinct sources of the various magmatic rock types.

The oxygen fugacity of magma reflects the redox state of magma and directly controls the crystallization sequence, composition and petrogenesis of magma. Together with temperature, pressure and melt composition, oxygen fugacity also controls the fluid composition, which has an impact on mineralization. This is particularly obvious in porphyry copper (gold) deposits. Arc magmas in subduction zones are generally considered to be water-rich and oxidized, and highly oxidized magma has the potential to assimilate sulfates during ascension (Sillitoe & Thompson, 2010). There are a number of porphyry Cu–Au–Mo

deposits related to oxidized calc-alkaline granitoids (Shen *et al.* 2016; Shu *et al.* 2019) in the CAOB. The study of our samples in the eastern CAOB can further evaluate the relationship between $f\text{O}_2$ and mineralization. At present, the calculation of the oxygen fugacity of magmatic rocks is mainly determined by the variable valence elements in minerals, by using the relationship between $\text{Fe}^{3+}/\text{Fe}^{2+}$ and temperature in the melt (Blevin & Chappell, 1992) or by using the $\text{Ce}^{4+}/\text{Ce}^{3+}$ ratio of zircon (Ballard *et al.* 2002). In our research, the oxygen fugacity is calculated by using the zircon Ce or Eu anomaly and zircon Ti temperature. However, the $f\text{O}_2$ values generated by the above methods can be scattered. We identify the possible causes and compare the oxygen fugacity values calculated by several different methods created by Smythe & Brenan (2016) and Loucks *et al.* (2020).

In this paper, we present new geochronological, petrological, geochemical, zircon Hf isotopic and whole-rock Li isotopic data for the middle–late Permian magmatic rocks in the Gongzhuling area, southwestern Jilin Province, NE China. Our aim was to identify the source characteristics of a typical magmatic suite, using zircon Hf isotopes, zircon oxygen fugacity and geochemical data for the Gongzhuling area during the middle–late Permian tectonic evolution of NE China, as well as test the effectiveness of Li isotopes in magma petrogenesis.

2. Geological setting

NE China is generally considered to comprise six microcontinental blocks: the Erguna and Xing'an blocks in the northwest, the Songliao Block in the centre and the Jiamusi Massif, Khanka Massif and Nadanhada Terrane in the southeast (Fig. 1b; Wu *et al.*

2011). The southward and northward subduction of the Palaeo-Asian oceanic plate induced the amalgamation of multiple terranes during Palaeozoic time, as evidenced by the E–W-striking Carboniferous–Permian intrusive magmatic belts along two sides of the Solonker Suture Zone (Ruzhentsev & Pospelov, 1992; Chen *et al.* 2009). The northwestward subduction of the western Pacific oceanic plate was accompanied by continental margin accretion during the Mesozoic–Cenozoic period, intense Mesozoic volcanic and intrusive activity, and the production of large volumes of alkaline basalt in Cenozoic time (Wang & Mo, 1995; Wu *et al.* 2000).

Voluminous Palaeozoic and Mesozoic granitoids and coeval mantle-derived mafic intrusions occur in NE China, including those along the suture zones between different blocks (Fig. 1b; Jahn, 2000; Zhang *et al.* 2004; Wang *et al.* 2017). Most of the Palaeozoic and Mesozoic granitoids in NE China are I- and A-types with low initial $^{87}\text{Sr}/^{86}\text{Sr}$ values (0.6919–0.7116), high $\epsilon_{\text{Nd}}(t)$ and $\epsilon_{\text{Hf}}(t)$ values, and young Nd and Hf T_{DM} ages (1265–643 Ma; Wu *et al.* 2000), and many previous researchers have indicated that the source areas of these granitoids contain large proportions of juvenile crustal material (Wu *et al.* 2000; Jahn *et al.* 2001, 2004; Kovalenko *et al.* 2004; Chen & Arakawa, 2005; Wang *et al.* 2015a). It has been proposed, therefore, that there was extensive crustal growth in this region during Mesoproterozoic and Neoproterozoic times (Sun *et al.* 2017).

The Gongzhuling area is located in southwestern Jilin Province, south of the Solonker–Xra Moron–Changchun Suture and north of the Bayan Obo–Chifeng–Kaiyuan Fault (the northern boundary fault of the North China Craton), on the SE margin of the Songliao Block (Fig. 1a). The Xra Moron–Changchun Suture is considered to represent the final closure zone of the Palaeo-Asian Ocean, as well as the youngest amalgamation of the North China Block and the Khanka Massif in the eastern CAOB (Zhang *et al.* 2014; Xu *et al.* 2015). The study area is situated in a Palaeozoic accretionary belt (Zhang *et al.* 2014; Ma *et al.* 2020), termed the Liaoyuan Terrane (Wu *et al.* 2011) or Liaoyuan Accretionary Belt (Li *et al.* 2021), allegedly the eastern extension of the Bainaimiao accretionary arc belt accreted to the northern margin of the North China Craton from late Silurian to Early Devonian times by arc–continental collision (Fig. 1b; Zhang *et al.* 2014). Previous results show that the granitoids in this area were emplaced mainly in three distinct stages: Permian to Early Triassic (285–245 Ma), Late Triassic to Middle Jurassic (210–155 Ma) and Early Cretaceous (135–100 Ma) (Wu *et al.* 2011; Ma *et al.* 2019). The host rocks are mainly metamorphosed (greenschist to lower-amphibolite facies) and deformed Palaeozoic sedimentary and volcanic rocks (Shao & Tang, 1995; Zhang *et al.* 2014). Some early Palaeozoic hornblende gabbro, quartz diorite and tonalite (Zhang *et al.* 2014; Ma *et al.* 2020) and Mesoproterozoic granitoids have recently been identified from this area (Li *et al.* 2021).

3. Sample descriptions

Collected from east of Gongzhuling City (Fig. 1c), the Gongzhuling dacite tuff samples (09326-1 and 09327-1) are grey (Fig. 2a) with crystal pyroclasts (~20% plagioclase, ~5% K-feldspar, ~3% quartz) and lithic fragments (~5%) cemented by volcanic ash (Fig. 3a).

Samples of pyroxene diorite (09335-1 and 09343-1; Fig. 2b, c), diorite (09331-1 and 09340-2; Fig. 2d), quartz monzodiorite (09346-1; Fig. 2e) and biotite syenogranite (09328-1; Fig. 2f) were collected from southeast of Gongzhuling City where these rocks

had been intruded into the Mesoproterozoic, early Palaeozoic or Devonian–Carboniferous metamorphosed volcanic–sedimentary rocks (Fig. 1c). The igneous rocks are grey to dark green, and coarse grained in texture (Fig. 3b, c). The dioritic rocks are equigranular, and the biotite syenogranite is hypidiomorphic (Fig. 3b–f). The pyroxene diorites are composed of clinopyroxene (25–30%), hornblende (25–35%) and plagioclase (35–45%). The diorites consist mainly of hornblende (35–50%), plagioclase (35–45%), biotite (5–8%), quartz (~1%) and titanite (~1%). The quartz monzodiorite is composed mainly of plagioclase (45–55%), hornblende (10–15%), K-feldspar (15–20%) and quartz (5–8%). The biotite syenogranite consists mainly of K-feldspar (35–45%), quartz (25–30%), plagioclase (15–20%) and biotite (8–10%). Main accessory minerals are apatite, titanite, epidote, zircon and magnetite (Fig. 3e).

The clinopyroxenes and hornblendes in these rocks are typically euhedral, suggesting early crystallization; grains of magnetite are commonly enclosed in the hornblende (Fig. 3c, d), also suggesting an earlier phase than the hornblende. The plagioclases are commonly euhedral to subhedral, suggesting later crystallization than the clinopyroxene (Fig. 3b). Quartz is mostly interstitial to the earlier crystallized feldspar and hornblende, indicating its late-stage crystallization. The euhedral wedge shapes of the titanite indicate its early crystallization (Fig. 3e).

4. Analytical methods

4.a. Zircon U–Pb dating and trace-element analyses

Zircons from eight rock samples (09326-1, 09328-1, 09331-1, 09333-1, 09335-1, 09340-2, 09343-1 and 09346-1) were selected for U–Pb dating. Zircon grains were separated from the fresh rock samples by traditional crushing, heavy liquid and magnetic methods, and the grains were then manually handpicked under a binocular microscope. Zircons were attached to an epoxy base and polished to expose the cores of the grains. Photomicrographs and cathodoluminescence (CL) images were used to assess the interior structures of the zircons for *in situ* U–Pb dating, Lu–Hf isotope analyses and zircon trace-element analyses.

Zircons U–Pb and trace-element analyses were conducted using laser ablation inductively coupled plasma mass spectrometry (LA-ICP-MS) with a 193 nm laser at the State Key Laboratory of Geological Processes and Mineral Resources, China University of Geosciences, Wuhan, China. The U–Pb dating experiments were performed on an Agilent 7500a ICP-MS (Agilent Technology, Yokogawa, Japan) coupled with a 193 nm ArF excimer laser denudation system (GeoLas 2005, Coherent Lambda Physik GmbH, Gottingen, Germany). The techniques we used have been described by Liu *et al.* (2010). Locations for the U–Pb analyses were selected on the basis of CL images and photomicrographs. Reference zircon 91500 was selected for age calibrations. GEMOC GJ-1 reference zircon (thermal ionization mass spectrometry (TIMS) U–Pb age = 608.5 ± 0.4 Ma; Jackson *et al.* 2004) was used as a monitor of data quality. The weighted mean ^{206}Pb – ^{238}U ages of reference zircons 91500 and GJ-1 were 1061 Ma and 606 Ma, respectively (online Supplementary Material Table S1), which are identical to those in the TIMS method (Jackson *et al.* 2004). The instrument was optimized with standard glass NIST SRM 610, and this glass was also used as a reference for calibration of the trace-element contents. ^{29}Si was used as an internal standard. Calculations of the trace-element concentrations were conducted using ICP-MS DataCal software (Liu *et al.* 2008). The zircon age calculations and concordia diagrams were made



Fig. 2. (Colour online) Photographs of outcrops showing different rock types of the Gongzhuling intermediate–felsic rocks. (a) Dacite tuff (43° 34.81' N, 125° 06.23' E). (b) Pyroxene diorite (43° 27.14' N, 125° 54.86' E). (c) Pyroxene diorite (43° 26.55' N, 124° 56.19' E). (d) Diorite (43° 27.28' N, 125° 00.24' E). (e) Quartz monzodiorite (43° 24.11' N, 124° 52.13' E). (f) Biotite syenogranite (43° 30.58' N, 125° 12.17' E). Length of pen for scale is 15 cm; length of hammer for scale is 50 cm; diameter of coin for scale is 2.5 cm.

using Isoplot 3.0 (Ludwig, 2003). Common Pb was corrected according to the method proposed by Andersen (2002).

4.b. Whole-rock major- and trace-element analyses

Whole-rock major- and trace-element analyses were performed at the Institute of Geology and Geophysics, Chinese Academy of Sciences, Beijing, China and at the State Key Laboratory of Geological Processes and Mineral Resources, China University of Geosciences, Wuhan. X-ray fluorescence was employed for the major-element analyses using fused glass discs of the sample powders. The analytical errors were less than 1%. Sample powders for trace-element analyses were dissolved in a diacid (15 mol L⁻¹ HNO₃ + 29 mol L⁻¹ HF) high-pressure vessel at 200 °C for four days and then dried. The dried powder was digested with HNO₃ at 150 °C for one day and then diluted to 50 ml with 1% HNO₃ for analysis determined by ICP-MS. Chinese national standards GSR-1 (granite) and GSR-3 (basalt) were used for monitoring and analysis. Except for P₂O₅ (5%), the analysis errors for the major elements are within 1%, while such errors for most trace elements (including rare earth elements (REEs)) are within 10%.

4.c. Zircon Lu–Hf isotopic analyses

In situ zircon Lu–Hf isotope analyses were conducted at the Institute of Mineral Resources, Chinese Academy of Geological Sciences, Beijing, China, using a Finnigan Neptune multicollector ICP-MS (MC-ICP-MS) coupled to a New Wave U P213 laser ablation system. The Hf isotope analyses were carried out beside the analytical points used for U–Pb dating with an ablation spot of 55 μm in diameter, and He was used as the carrier gas with a flow rate of 0.8–0.9 L min⁻¹. The reference zircon GJ-1 was used for calibration. Isobaric interference of ¹⁷⁶Lu on ¹⁷⁶Hf was adjusted according to the measurement of the ¹⁷⁵Lu value. The ¹⁷⁶Yb/¹⁷²Yb and mean β_{Yb} values were obtained during laser ablation on the same analytical spots as used for Hf isotope analyses, which allowed for correction of the interference of ¹⁷⁶Yb on ¹⁷⁶Hf (Wu *et al.* 2006).

4.d. Whole-rock Li isotope analyses

The separation of lithium for isotope analyses was performed by inorganic solvent-free two-step liquid chromatography in the ultra-clean laboratory of the University of Science and Technology of China, Hefei, China, following the method

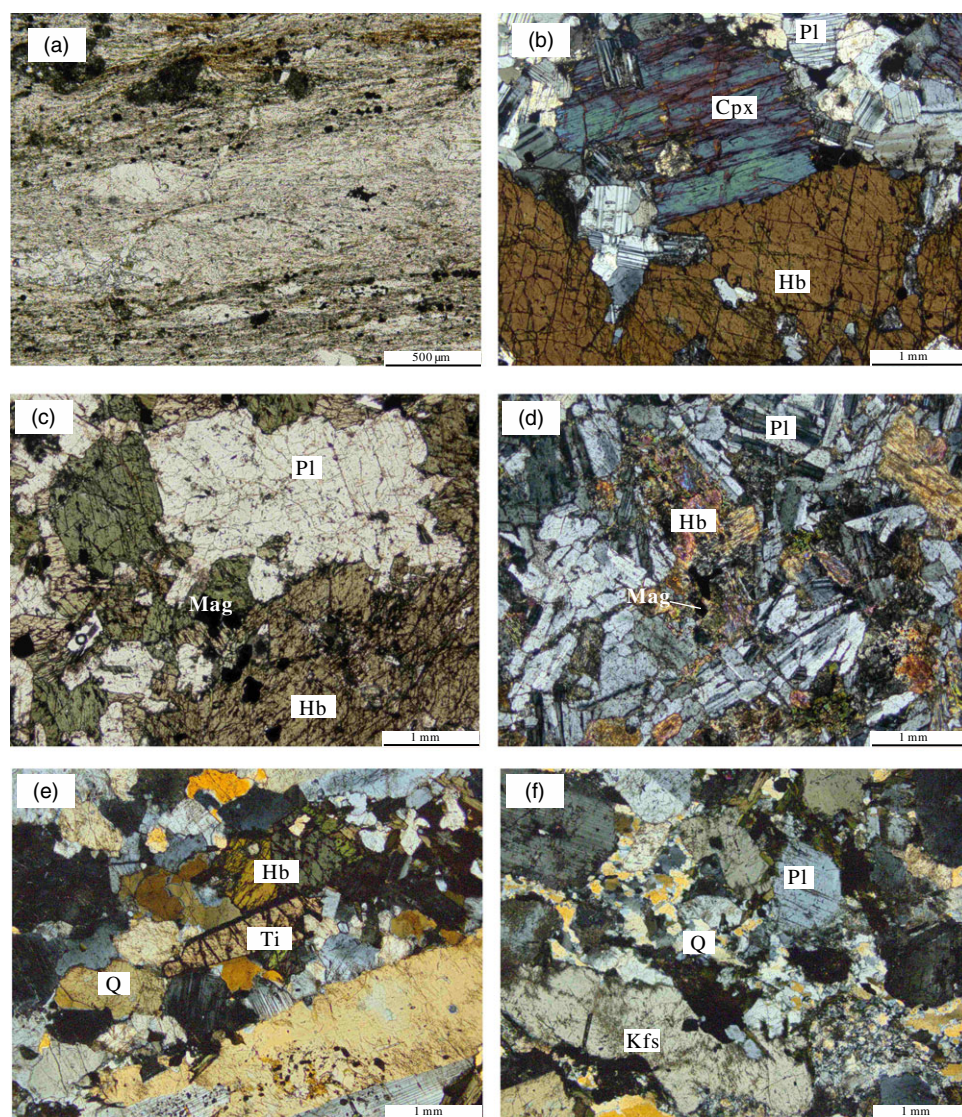


Fig. 3. (Colour online) Photomicrographs showing typical textures of the Gongzhuling intermediate-felsic rocks. (a) Dacite tuff (09326-1). (b) Pyroxene diorite (09335-1). (c) Diorite (09331-1). (d) Diorite (09340-2). (e) Quartz monzodiorite (09346-1). (f) Biotite syenogranite (09328-1). Cpx - clinopyroxene; Hb - hornblende; Pl - plagioclase; Ti - titanite; Kfs - K-feldspar; Q - quartz; Mag - magnetite.

described by Gao & Casey (2012). All the separation processes were assessed using ICP-MS analyses to ensure high Li yields (>99.8%) and low Na/Li values (<0.5). After the rock samples were dissolved by acid mixture of concentrated HF-HNO₃-HCl, approximately 200–5000 ng Li was loaded onto the column with Bio-Rad AG50W X12 resin. The matrix was then eluted with 0.2 N HCl solution to ~80 ml. The collected lithium was dried and treated with 2% nitric acid in a 50–100 ppb solution for analyses of the isotope compositions on a Neptune MC-ICP-MS. Collection of ⁶Li and ⁷Li was made with two Faraday cups (L4 and H4). The total procedural blank of the column procedure was not more than ~0.03 ng Li. In comparison to the 200–5000 ng Li of the samples, the procedural blank correction is insignificant at the uncertainty level reached. The Li isotopic compositions are presented as $\delta^7\text{Li} = ((^7\text{Li}/^6\text{Li})_{\text{sample}} / (^7\text{Li}/^6\text{Li})_{\text{standard}} - 1) \times 1000$ compared with the L-SVEC lithium isotopic standard (Flesch *et al.* 1973; Magna *et al.* 2006; Jeffcoate *et al.* 2007; Simons *et al.* 2010). According to the results, the reference samples were $+4.3 \pm 0.2$ ‰ for BHVO-2 (three samples) and $+7.0 \pm 0.1$ ‰ for AGV-2 (two samples), which were all within the uncertainty range of the previous published data (Rudnick *et al.* 2004; Magna *et al.* 2006; Simons *et al.* 2010).

5. Results

5.a. Zircon U-Pb ages

Most of the zircons are euhedral, stubby prisms in CL images that are 60 to 300 µm, and the crystals have tapered terminations and clear oscillating zoning (Fig. 4), indicating a magmatic origin (Pupin, 1980). Zircons without visible inclusions were selected for U-Pb isotopic dating. The Th and U contents and the U-Pb isotope values are presented in online Supplementary Material Table S1 and shown on concordia diagrams (Fig. 4). The zircons have a wide range of U concentrations from 51 to 2178 ppm (online Supplementary Material Table S1), and most of the Th/U values of individual zircon grains are between 0.3 and 1.0 (online Supplementary Material Table S1), indicating a magmatic origin for the analysed zircons (Kirkland *et al.* 2015).

As shown in Figure 4a–h, the analytical spots yielded well-defined ²⁰⁶Pb–²³⁸U concordant ages, which we consider to be emplacement ages. The ²⁰⁶Pb–²³⁸U ages of 11 analysed zircons from the dacite tuff (09326-1, Fig. 4a) range from 258 ± 2 to 267 ± 2 Ma (1σ), with a weighted mean ²⁰⁶Pb–²³⁸U age of 262 ± 2 Ma (MSWD = 2.3, 2σ). Analyses of 12 zircons from the

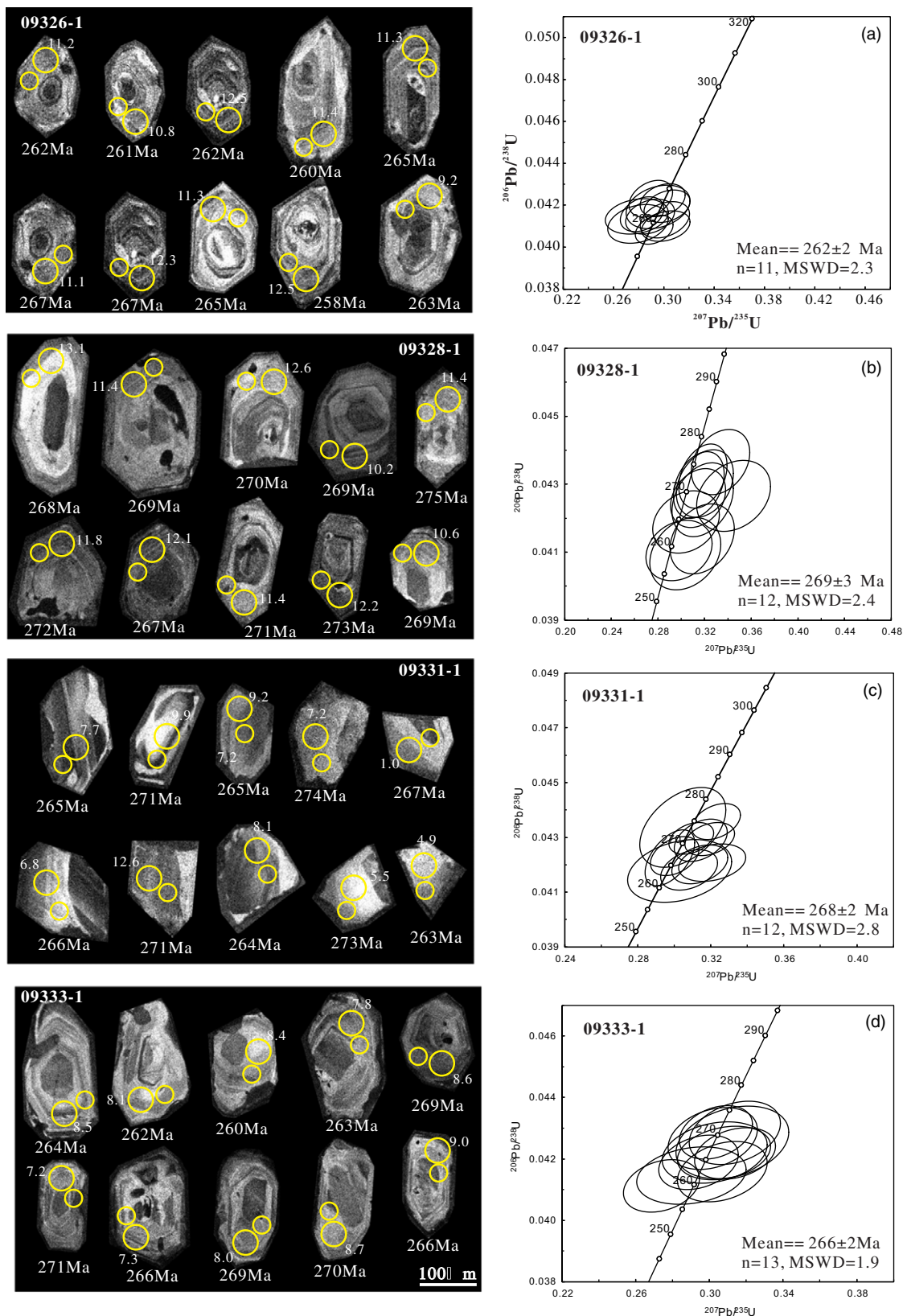


Fig. 4. (Colour online) Cathodoluminescence images of representative zircons and U-Pb concordia diagrams for the zircons from intermediate-felsic rocks in the Gongzhuling area. The small yellow circles are U-Pb dating spots and the large circles represent locations of Hf isotopic analyses. The data beside the large circles are $\epsilon_{\text{Hf}}(t)$ values.

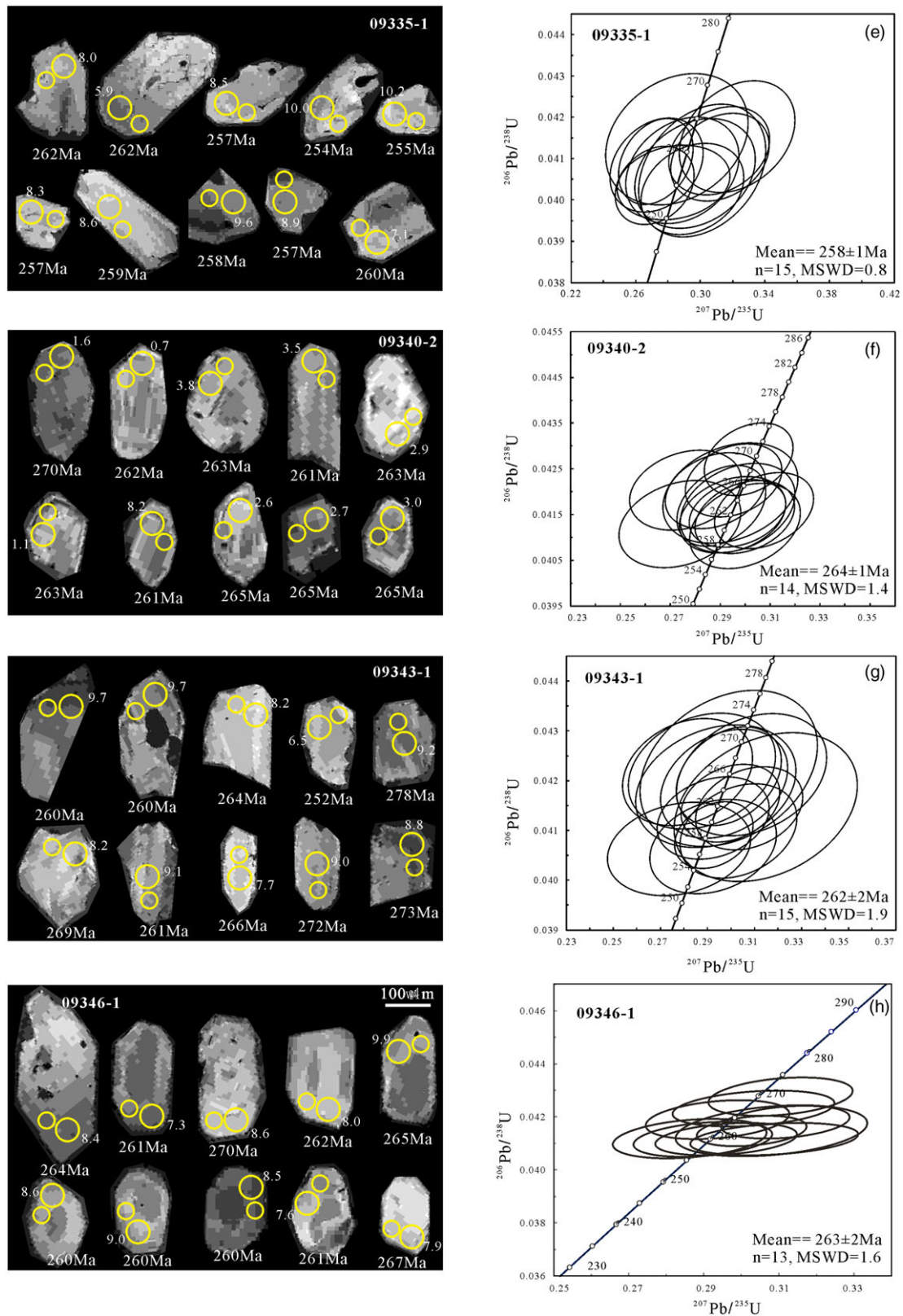


Fig. 4. (Colour online) (Continued).

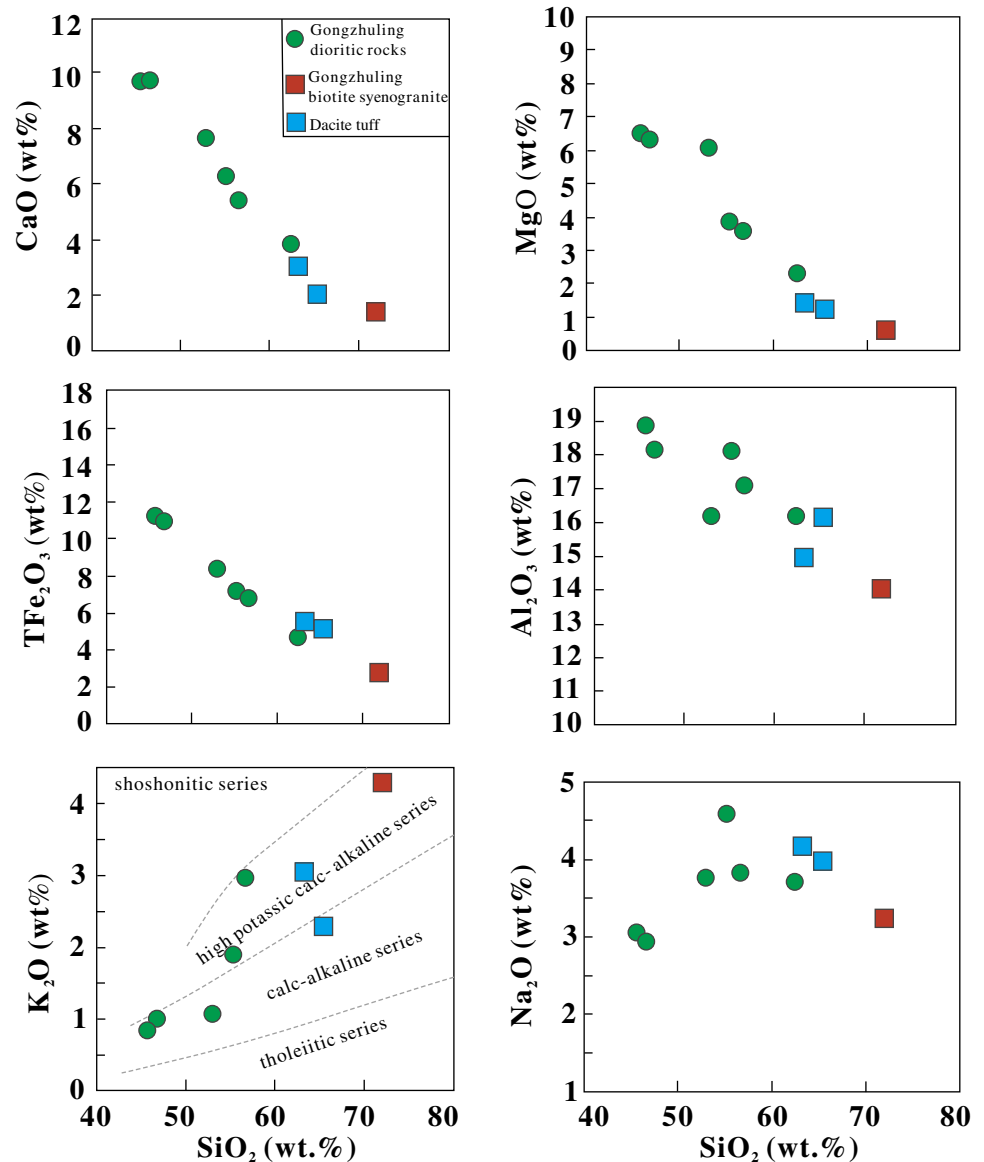


Fig. 5. (Colour online) Harker diagrams for the intermediate-felsic rocks in the Gongzhuling area.

biotite syenogranite (09328-1, Fig. 4b) yielded ^{206}Pb – ^{238}U ages ranging from 261 ± 3 to 275 ± 2 Ma (1σ), with a weighted mean ^{206}Pb – ^{238}U age of 269 ± 3 Ma (MSWD = 2.4, 2σ). For diorite sample 09331-1 (Fig. 4c), 12 analyses of zircons yielded ^{206}Pb – ^{238}U ages ranging from 264 ± 2 to 274 ± 2 Ma (1σ), with a weighted mean ^{206}Pb – ^{238}U age of 268 ± 2 Ma (MSWD = 2.8, 2σ), and for diorite sample 09333-1 (Fig. 4d), 13 analyses yielded ^{206}Pb – ^{238}U ages between 260 ± 2 and 271 ± 2 Ma (1σ), with a weighted mean ^{206}Pb – ^{238}U age of 266 ± 2 Ma (MSWD = 1.9, 2σ). For pyroxene diorite sample 09335-1 (Fig. 4e), 15 analyses of zircons yielded ^{206}Pb – ^{238}U ages ranging from 254 ± 3 to 265 ± 4 Ma (1σ), with a weighted mean ^{206}Pb – ^{238}U age of 258 ± 1 Ma (MSWD = 0.8, 2σ). Diorite sample 09340-2 (Fig. 4f) yielded 14 zircon ^{206}Pb – ^{238}U ages ranging from 261 ± 2 to 270 ± 2 Ma (1σ), with a weighted mean ^{206}Pb – ^{238}U age of 264 ± 1 Ma (MSWD = 1.4, 2σ). The 15 analysed zircons from pyroxene diorite sample 09343-1 yielded ^{206}Pb – ^{238}U ages between 257 ± 2 and 267 ± 4 Ma (1σ), with a weighted mean ^{206}Pb – ^{238}U age of 262 ± 2 Ma (MSWD = 1.9, 2σ) (Fig. 4g). For quartz monzodiorite sample 09346-1, 13 zircon analyses yielded ^{206}Pb – ^{238}U ages ranging from 260 ± 3 to 270 ± 3 Ma (1σ), with a

weighted mean ^{206}Pb – ^{238}U age of 263 ± 2 Ma (MSWD = 1.6, 2σ) (Fig. 4h). These dating results show that the dacite tuff and the intermediate-felsic intrusions in the Gongzhuling area were formed during middle-late Permian (269–258 Ma) time.

5.b. Major and trace elements

The major- and trace-element compositions of the intermediate-felsic Permian intrusions are given in online Supplementary Material Table S3. They have a wide range of compositions, with $\text{SiO}_2 = 45.7$ – 71.9 wt %, $\text{Al}_2\text{O}_3 = 14.1$ – 18.9 wt %, total $\text{Fe}_2\text{O}_3 = 2.7$ – 11.2 wt % and $\text{MgO} = 0.6$ – 6.5 wt %, and relatively high contents of Na_2O (3.0–4.6 wt %). Al_2O_3 , Fe_2O_3 , MgO and CaO decrease with increasing SiO_2 on Harker diagrams (Fig. 5), whereas K_2O increases with increasing SiO_2 . Most of the samples plot in the medium- to high-K field on the K_2O versus SiO_2 diagram (Fig. 5).

With regard to their trace-element contents (Fig. 6), Sr shows a negative correlation with SiO_2 . Chondrite-normalized REE patterns of the intrusions show they are enriched in light REEs

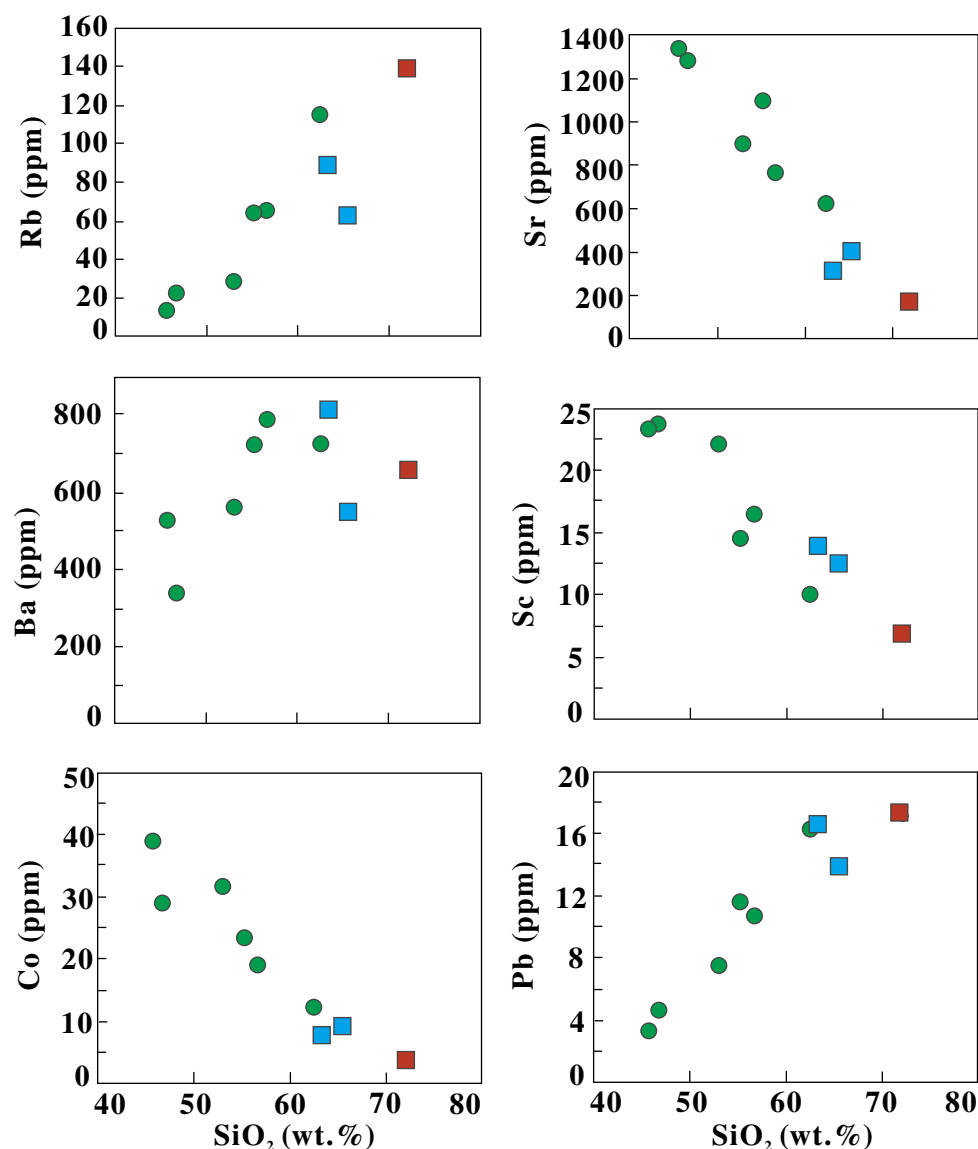


Fig. 6. (Colour online) Plots of selected trace-element contents versus silica contents for the intermediate-felsic rocks in the Gongzhuling area.

(LREEs) with values of La_N/Yb_N ranging from 5.1 to 22.0. They show slightly negative Eu anomalies, only biotite syenogranite showing a distinct Eu anomaly ($Eu/Eu^* = 0.5$; Fig. 7a). In a primitive mantle-normalized trace-element diagram, all the samples show enrichments in large-ion lithophile elements (LILEs) (e.g. Rb, Sr, Ba and Pb). They have obvious negative anomalies of the high field strength elements (HFSEs) of Ti, Nb, Ta, Zr and Hf, which are the features of subduction-related rocks (Hawkesworth *et al.* 1991; Fig. 7b). The depletion of the HFSEs Nb and Ti in our samples suggests that the enriched feature is subduction-related (Thirlwall *et al.* 1994).

5.c. Lu-Hf and Li isotopic compositions

The zircon Lu-Hf isotopic data are listed in online Supplementary Material Table S4 and plotted in Figure 8. The Hf isotope analyses for 15 zircon grains from the dacite tuff (09326-1) yielded $\epsilon_{Hf}(t)$ values ranging from 8.4 to 12.5. Fifteen zircons from the biotite syenogranite (09328-1) yielded $\epsilon_{Hf}(t)$ values of 9.9 to 13.1. The zircons from the dioritic specimens (09331-1, 09333-1, 09335-1,

09340-2, 09343-1, 09346-1) yielded $\epsilon_{Hf}(t)$ values of 0.7 to 13.1 (Fig. 8b). The calculated depleted mantle Hf model ages (T_{DM2}) of all the samples range from 458 to 1251 Ma (online Supplementary Material Table S4).

The Li isotopic compositional data are listed in online Supplementary Material Table S5 and shown in Figure 9. The samples have variable Li contents that range from 7.5 ppm to 28.6 ppm. The middle-late Permian biotite syenogranite (09328-1) has $Li = 30.7$ ppm and $\delta^7Li = +1.28$. The middle-late Permian diorites (09331-1, 09333-1 and 09340-2) have $Li = 13.5$ – 19.4 ppm and $\delta^7Li = +1.4$ to $+3.5$. The middle-late Permian pyroxene diorites (09335-1 and 09343-1) have Li contents of 9.6 and 8.0 ppm and δ^7Li values of $+2.4$ and $+0.4$, respectively. The middle-late Permian dioritic rock (09346-1) has $Li = 19.4$ ppm and $\delta^7Li = +0.61$. As shown in Figure 9, the Li contents and δ^7Li values of our samples are similar to those of typical I-type granites (Bryant *et al.* 2004; Teng *et al.* 2004; Magna *et al.* 2010), but they differ from S-type granites (Bryant *et al.* 2004; Teng *et al.* 2006; Magna *et al.* 2010; Romer *et al.* 2014; Chen *et al.* 2018), which usually feature higher Li and lower δ^7Li values.

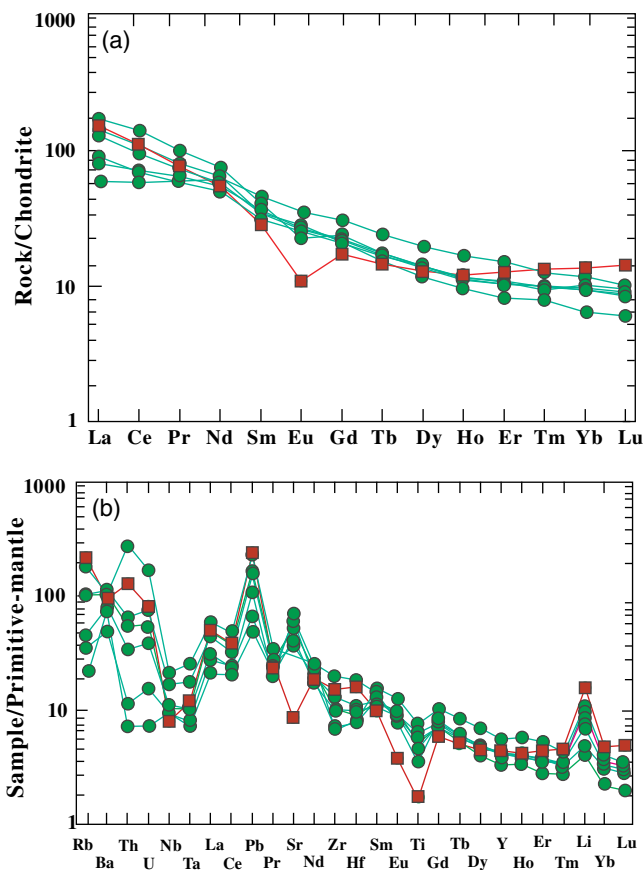


Fig. 7. (Colour online) (a) Chondrite-normalized REE and (b) primitive-mantle-normalized trace-element variation diagrams for the middle-late Permian intermediate-felsic rocks in the Gongzhuling area. Chondrite and primitive mantle values are from Boynton (1984) and Sun & McDonough (1989), respectively.

6. Discussion

6.a. Petrogenesis of the middle-late Permian magmatic rocks

The Gongzhuling intermediate-felsic intrusions are high-K and calc-alkaline with Mg no. values of 31.3–59.1. They share features with continental-arc magmas, such as their calc-alkaline compositions, enrichments in LILEs (e.g. Rb, Sr and Ba) and depletions in HFSEs (e.g. Nb, Ta, Zr and Hf) (Claeson & Meurer, 2004).

We believe that magma mixing was involved in the formation of the dioritic rocks (samples 09331-1, 09333-1, 09340-2 and 09346-1). The reasons include: (1) Their Mg no. values (49.6–59.1) are higher than those of experimental basalt melts with the same SiO₂ contents (Mg no. <42; Rapp & Watson, 1995). This precludes partial melting of the lower crust as the sole source of these intrusive rocks, because mixing with a high-Mg mantle-derived mafic magma is required. (2) Their zircons have variable Hf isotopic ratios (although they have roughly the same U–Pb ages; Fig. 8), and this is seen in many other plutons formed through magma mixing processes (Kemp *et al.* 2006). (3) The negative correlation between SiO₂ and Sr (Fig. 6) suggests that the high LILE contents (e.g. Sr = 627–1340 ppm) were inherited from mafic magmas derived from a metasomatized mantle, as crust-derived melts typically have a low Sr content (< 300 ppm; Rapp & Watson, 1995). As the heavy REE (HREE) depletion with respect to medium REEs (MREEs) exhibited by the granodiorites of the study is not as

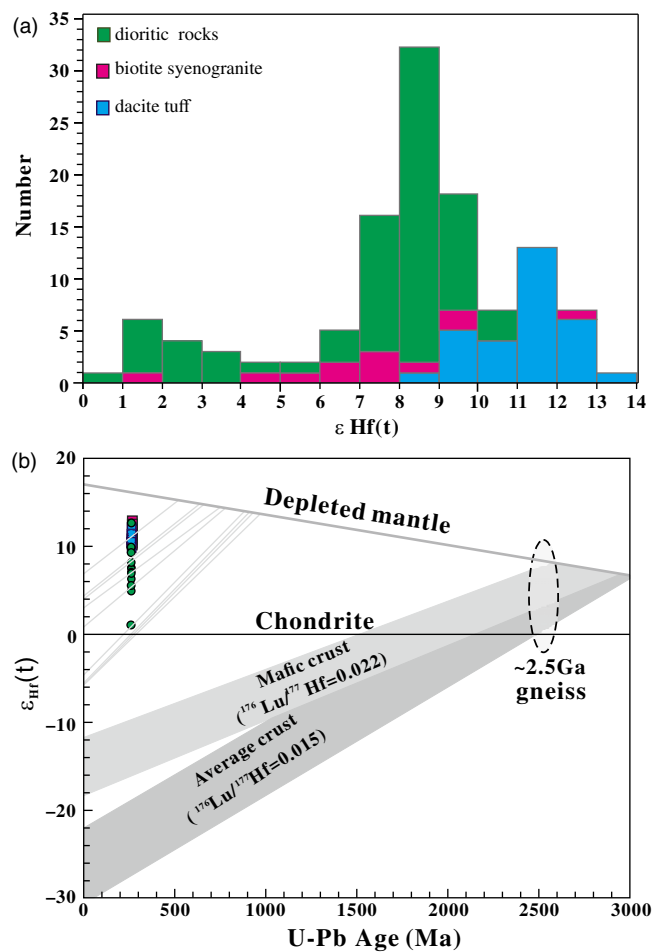


Fig. 8. (Colour online) Zircon Lu–Hf isotopes of the Gongzhuling middle-late Permian magmatic rocks. (a) Histogram of ε_{Hf}(t) values. (b) ε_{Hf}(t) versus U–Pb zircon ages.

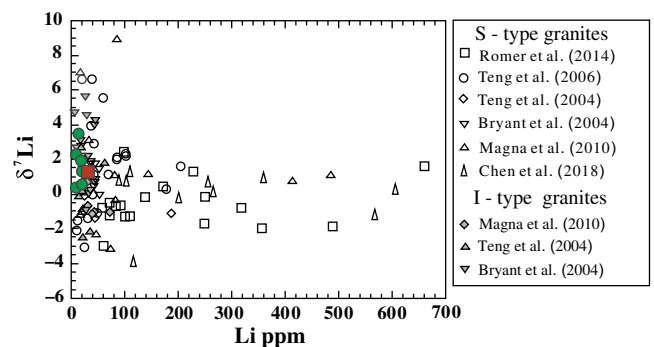


Fig. 9. (Colour online) Plot of δ⁷Li versus Li for the intermediate-felsic rocks in the Gongzhuling area. Also shown for comparison are data for global S- and I-type granites.

prominent as in melts derived from thickened eclogitic lower crust, which feature higher Sm/Yb ratios (Rapp & Watson, 1995), our samples are not likely to be the partial melts of thickened eclogitic lower crust. The linear relationships between SiO₂ and Ba, Sr and Rb are indicative of magma mixing or fractionation of biotite instead of intensive plagioclase crystallization, as was proved by weak Eu anomalies. Mixing between granitic and mafic magmas can produce hybrid magmas whose data points plot continuously

between the two end-members (Gerdes *et al.* 2000; Chen & Arakawa, 2005; Janoušek & Moyer, 2020).

The most mafic sample (pyroxene diorite 09343-1) cannot represent a primary basaltic magma derived from the melting of the mantle wedge, because its MgO content (6.51 wt %) is lower than that of typical primitive arc basalt (9.86 wt %; Sisson & Grove, 1993). However, our samples of pyroxene diorite underwent minor crustal contamination, as they show small variations (up to four ϵ_{Hf} units) in ϵ_{Hf} values (online Supplementary Material Table S4). The end-member of a basaltic melt could be represented by the olivine gabbros (273 Ma) that occur in the adjacent region, and which have $\epsilon_{\text{Hf}}(t) = +5.6$ to $+14.6$ and $\epsilon_{\text{Nd}}(t) = +0.9$ to $+6.8$ (Li *et al.* 2010; Guo *et al.* 2015), and were considered to be derived from a metasomatized mantle wedge. However, there is a lack of Palaeozoic primitive arc basalts related to subduction in NE China owing to post-orogenic unroofing and erosion (Guo *et al.* 2015), and thus the only way to evaluate the geochemical features of the mantle source is by estimating the compositions of the parental magmas of these mafic intrusions.

The mantle source was a mantle wedge that had been enriched in trace elements. The olivine gabbros in the region are enriched in LILEs (e.g. K, Rb, Sr, Ba and Pb) and LREEs, and depleted in HFSEs (e.g. Nb and Th) (Li *et al.* 2010; Guo *et al.* 2015) and have depleted Sr–Nd–Hf isotopic features, similar to our dioritic samples. The negative correlation between SiO_2 and Sr (Fig. 6) of our dioritic samples suggests that the high contents of LILEs (e.g. K, Rb, Sr and Ba) stemmed from the metasomatized mantle, because crust-derived melts typically have a low Sr content (<300 ppm; Rapp & Watson, 1995). This inference is supported by the negative anomalies of HFSEs (e.g. Nb, Ta, Zr and Hf) in the intrusive rocks (Fig. 8b). The mantle source was isotopically depleted, because ϵ_{Hf} (260 Ma) values (+0.7 to +13.1) are positive. The decoupling of depleted Hf isotopes and enriched elemental signatures indicates that partial melting of the mantle wedge occurred shortly after its metasomatism so that the accumulation of radioisotopes was insufficient. Basaltic magma with depleted isotopic characteristics would have been formed by partial melting of the newly enriched mantle wedge above the subducted slab (Chen & Arakawa, 2005). The young Hf T_{DM2} model ages ($T_{\text{DM2}} = 0.46\text{--}1.2$ Ga; online Supplementary Material Table S4) should be the formation age of the juvenile arc basalt.

Although the middle–late Permian Gongzhuling intermediate rocks exhibit a wide range of geochemical compositions, the overall trends of the dioritic rocks on Harker diagrams are regular (Figs 5, 6), reflecting a genetic link within these rocks. This inference is further supported by their similar REE patterns (Fig. 7a) and spider diagrams (Fig. 7b). Most of the samples show clear linear relationships between SiO_2 and CaO, MgO, TFe_2O_3 , Al_2O_3 , Rb, Ba, Sc, Sr, Co and Pb (Figs 5, 6), indicating the significant role of fractional crystallization in the evolution of the magma. CaO, MgO and TFe_2O_3 show a negative correlation with SiO_2 (Fig. 5), indicating that pyroxene, amphibole and other ferromagnesian phases underwent significant fractionation, which is consistent with the negative correlation between SiO_2 and the contents of Co and Sc (Fig. 6).

The biotite syenogranite (sample 09328-1) could represent crust-derived melts rather than the differentiation of dioritic melts via fractionation of ferromagnesian minerals such as pyroxene and hornblende. The Sr content of the biotite syenogranite is 176 ppm, similar to that of the melts of the lower crust (Petford & Gallagher, 2001), and much lower than the dioritic intrusions

(Sr = 627–1340 ppm; online Supplementary Material Table S3). The granite has a low Mg no. value, is enriched in LREEs and LILEs, and depleted in HFSEs (Nb, Ta and Ti; Fig. 7), which suggests the parental magma was produced by the partial melting of crustal material. To determine whether the biotite syenogranite was fractionated from the dioritic rocks, we conducted a test based on the Rayleigh fractionation law (Rollinson, 1993) using trace elements (e.g. Sr, Rb and Ba). The biotite syenogranite shows negative Eu anomalies ($\text{Eu}/\text{Eu}^* = 0.5$) and enrichments in LREEs compared with MREEs ($(\text{La}/\text{Sm})_{\text{N}} = 5.09$), suggesting significant fractionation of hornblende and plagioclase. We find that 10 % fractionation of the assemblage Hb (15 %) + Pl (50 %) + Kfs (35 %) from the most evolved dioritic sample (09333-1) could have formed the biotite syenogranite, based on the Rb and Ba contents (online Supplementary Material Table S3). However, this is at odds with the Sr data for the biotite syenogranite, as the fractionation assemblage would have led to a substantially higher Sr content in the residual magma than that found in the actual biotite syenogranite (online Supplementary Material Table S3). We conclude, therefore, that the biotite syenogranite is more likely to represent a partial melt of the lower crust rather than the fractional crystallization of the dioritic magma. Considering the highly depleted $\epsilon_{\text{Hf}}(t)$ values of the biotite syenogranite (+10 to +13) and its enrichment in LILEs, we propose that the lower-crustal source was dominated by depleted arc basalts. The crustal source could have been a juvenile (Neoproterozoic) underplated arc basalt, and this is supported by the young T_{DM2} model ages ($T_{\text{DM2}} < 1.2$ Ga; online Supplementary Material Table S4) given by the zircon Hf isotopic data.

6.b. Li isotopic composition of the source region

Previous research has shown the potential use of Li isotope studies in tracking crust–mantle evolution, as the weathered upper crust is characterized by light Li isotopic compositions ($\delta^7\text{Li} = -5.0$ ‰ to 5.0 ‰; Teng *et al.* 2004), while the heavy Li flows into the ocean via rivers. Lithium can be fractionated during hydrothermal alteration or surface weathering because ^7Li is preferentially partitioned into the fluid phase during surface processes (Wunder *et al.* 2006). There is a fixed Li isotopic fractionation between the newly formed clay minerals and seawater ($\Delta_{\text{seawater-clay mineral}} \approx 16\text{--}19$ ‰) during alteration (Chan *et al.* 2002). Clay minerals tend to extract more ^6Li than ^7Li from the seawater in low-temperature alteration, leading to altered oceanic crust with heavy Li isotopic compositions ($\delta^7\text{Li} = +7$ to $+14$ ‰; Berger *et al.* 1988; Chan & Kastner, 2000; Vigier *et al.* 2008). The subsequent subduction of the altered oceanic crust transports some of the heavy Li into the source of arc magmas by the release of fluids, which was considered short-lived in the early stage of subduction (John *et al.* 2012). According to previous models (Zack *et al.* 2003; Elliott *et al.* 2004), Marschall *et al.* (2007) predicted that the fore-arc mantle wedge is enriched in Li and has distinctly higher $\delta^7\text{Li}$ values than average mantle does. $\delta^7\text{Li}$ values are controlled mainly by the source region, and barely affected by such factors as metamorphic events, crustal anatexis and magmatic crystallization (Tomascak *et al.* 1999; Teng *et al.* 2004, 2006; Magna *et al.* 2006; Wunder *et al.* 2006).

The complexity of dehydration and metamorphism of the subducted slab adds to the controversy about Li isotopic fractionation. On the one hand, Zack *et al.* (2003) believed that there is strong Li isotopic fractionation during the process of low-temperature dehydration melting of the slab in the early stage of subduction, using the open-system Rayleigh fractionation model. In the existing data

of rock samples, only the $\delta^7\text{Li}$ value of alpine eclogite in an orogenic belt is smaller than that of the upper continental crust, indicating that the subducted plate lost heavy Li in the process of metamorphism and dehydration (Zack *et al.* 2003). On the other hand, Dohmen *et al.* (2010) maintained that Li is removed from the fluid to mantle mainly by diffusion when the pressure–temperature exceeds the Li-rich mineral (e.g. chlorite, serpentine, talc) stability region, and the relationship between Li isotopic diffusion rate and temperature is: $\lg D_{\text{Li}} = -5.92(\pm 1.0) - 1.2847 \times 10^4/T(\text{K})$. Li^+ and Mg^{2+} have a similar ionic radius, and Li^+ can replace Mg^{2+} in olivine, enstatite and diopside (Chan *et al.* 1992), thus extracting Li from subduction fluid. Li has a fast and slow diffusion rate in different positions of the lattice, since Li in experimental olivine (800–1200 °C, 100 KPa, $f\text{O}_2 \approx \text{WM}$ buffer) was supposed to partition between an octahedrally coordinated Mg site (Li_{Me}) and an unoccupied octahedral interstitial site. Li occupies the two different positions, and during diffusion the concentrations of Li in the two sites interact with each other by a homogeneous exchange reaction ($\text{Li}_{\text{Me}} = V_{\text{Me}} + \text{Li}_{\text{i}}$; Li_{i} , Dohmen *et al.* 2010). The diffusion of ^6Li is 3 % faster than that of ^7Li in basaltic and rhyolitic melts (Richter *et al.* 2003). Thus, the diffusion can lead to significant Li isotopic fractionation under the condition of high temperatures of 800–1200 °C. However, according to Teng *et al.* (2007), the Li isotopes hardly change during metamorphic dehydration, because the Li isotopic change of the Onawa metapelites is insignificant (~ 3 ‰) in the process of contact metamorphism with the calculated fractionation factor $\alpha^{\text{fluid/rock}}$ of 1.000–1.004. More experiments are needed to verify the fractional calculation of Li isotopes in the subduction process. The accurate calculation of the release depth of Li in the fore-arc region and the behaviour of Li in the mantle wedge are yet to be studied.

Petrological observations (no low-temperature hydrothermal altered minerals) and low loss on ignition (LOI) values (0.68–1.6%; online Supplementary Material Table S3) indicate the Gongzhuling dioritic intrusions and biotite syenogranite underwent hardly any fluid alteration at or near the surface, and this is supported by no correlation between LOI and $\delta^7\text{Li}$ values or Ba/Nb values. The Ba/Nb values can indicate the degree of slab-derived metasomatism or lower-crust dehydration melting, as Ba is fluid-active whereas Nb is fluid-inactive, and lower-crust dehydration melting results in the depletion of LILEs (Rb, Ba and K), U and Pb, and enrichment of Th and Nb in magmatic rocks (Yogodzinski *et al.* 2001; Bourdon *et al.* 2002). The difference in coordination numbers among coexisting phases is the dominant factor controlling kinetic Li isotopic fractionation, as ^6Li has priority in the lattice site with the higher coordination number (Sartbaeva *et al.* 2004; Wunder *et al.* 2006; Magna *et al.* 2016), so that ^6Li replaces Mg in octahedrally coordinated clinopyroxene (Halama *et al.* 2011; Cahalan *et al.* 2014; Sun *et al.* 2016). Therefore, kinetic fractionation results in significant Li isotope fractionation at high temperatures (800–1200 °C), and, for magma, the more mafic, the lower the $\delta^7\text{Li}$ values. The negative correlation between $\delta^7\text{Li}$ and Ba/Nb of the dioritic rocks ($R^2 = 0.79$; Fig. 10a) reveals that the samples were mainly derived from dehydration melting of the mafic lower crust, because during dehydration melting, $\delta^7\text{Li}$ values increase but Ba/Nb decreases. The whole-rock geochemical data for the Gongzhuling intermediate rocks suggest that the magmas were mainly formed by melting of a juvenile lower crust, as discussed above. Therefore, dehydration melting processes had influenced the Li isotopic compositions of our samples.

The average Li contents of the upper crust, lower crust and mantle are 30.5, 13 and 1–2 ppm, respectively (Teng *et al.* 2008;

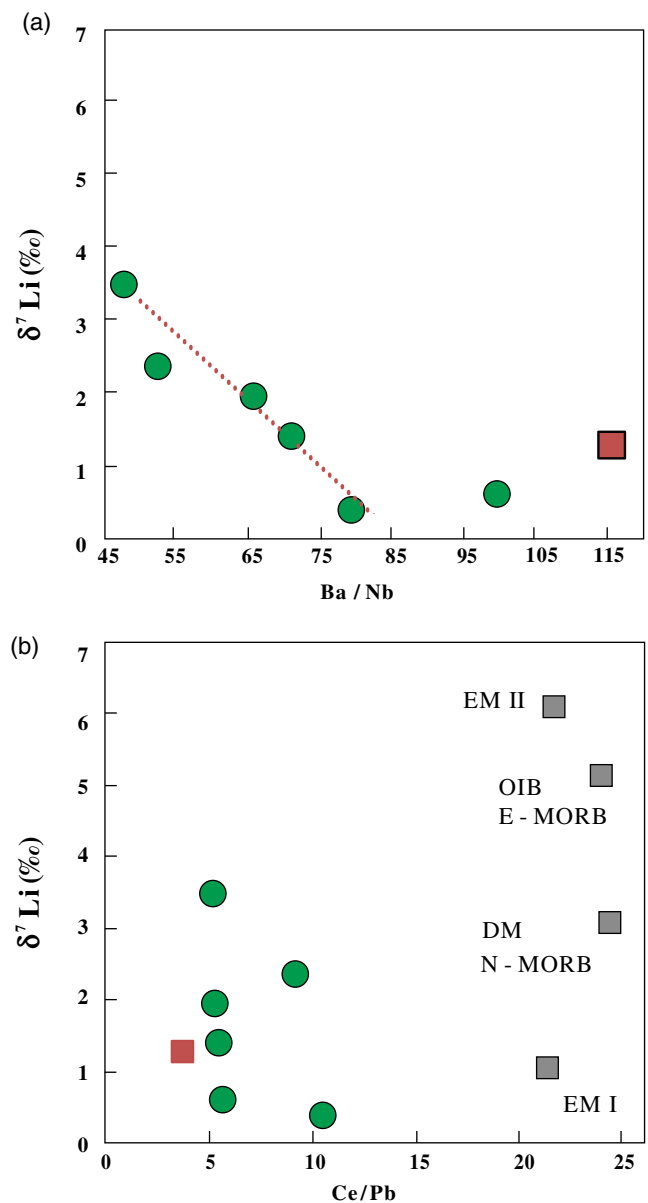


Fig. 10. (Colour online) Lithium isotopes versus trace-element compositions of the intermediate–felsic intrusive rocks in the Gongzhuling area. Also shown are mean compositional values for mantle end-members mid-ocean ridge basalt (MORB) and ocean island basalt (OIB) from Sun & McDonough (1989), Armienti & Gasperini (2007) and Nishio *et al.* (2007); subduction zone arc volcanic rocks from Miller *et al.* (1994) and Pearce *et al.* (1995). DM – depleted mantle; EM – enriched mantle.

Sauzéat *et al.* 2015). As shown in Figure 9, the Li concentrations in the Gongzhuling middle–late Permian intermediate intrusions exhibit a narrow range from 8.0 to 19.4 ppm with an average of 14.6 ppm (online Supplementary Material Table S5), similar to the average Li content of the lower continental crust (~ 13 ppm; Teng *et al.* 2008). Enriched mantle (EM) I-type melts usually have relatively small $\delta^7\text{Li}$ values (mean $\delta^7\text{Li} = +2.7$ ‰), possibly because of the recycling of subducted sediments (Zack *et al.* 2003). EM II-type melts usually have high $\delta^7\text{Li}$ values ($\delta^7\text{Li} = +6.3$ ‰), as oceanic crust absorbs heavy Li from seawater during low-temperature alteration (Magna *et al.* 2010). The melting of an enriched mantle wedge metasomatized by slab-released fluids can lead to heavy $\delta^7\text{Li}$ signatures. The lower continental crust contains variable $\delta^7\text{Li}$ values of between -17.9 ‰ and $+15.7$ ‰

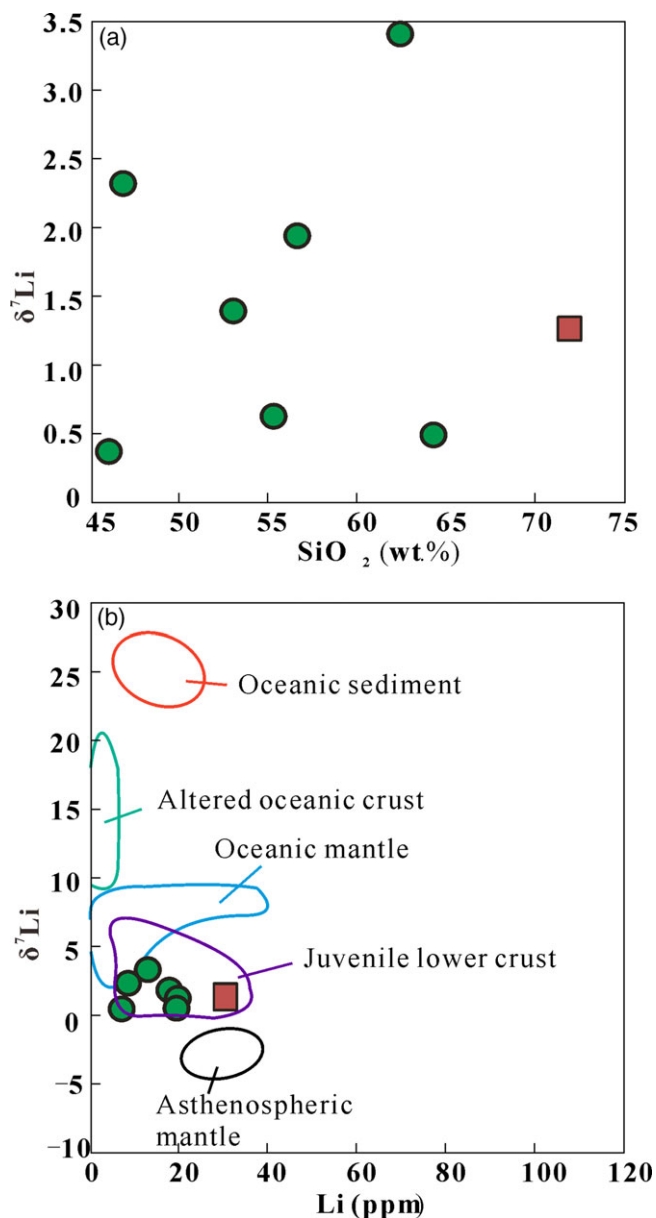


Fig. 11. (Colour online) Plots of (a) $\delta^7\text{Li}$ versus SiO_2 and (b) $\delta^7\text{Li}$ versus Li for the intermediate-felsic rocks in the Gongzhuling area. Data for mantle end-members are from Krienitz *et al.* (2012) and data for juvenile lower crust are from Tian *et al.* (2018). Data for altered oceanic crust are from Chan *et al.* (1992), Ryan & Langmuir (1987), Chan & Edmond (1988), Moriguti & Nakamura (1998) and Zack *et al.* (2003).

(Teng *et al.* 2008). The $\delta^7\text{Li}$ values in the Gongzhuling magmatic intrusions range from +0.4 to +3.5 ‰ with a mean of 1.6 ‰, similar to that of the juvenile lower crust (Li = 7.1–37.2, $\delta^7\text{Li}$ = +0.8–+6.6 ‰; Tian *et al.* 2018; Fig. 11b), thus precluding their direct derivation from the mantle wedge, as lithium does not fractionate during the formation and differentiation of basaltic magma (Tomascak *et al.* 1999).

Wall-rock assimilation or contamination may also change the Li concentration and $\delta^7\text{Li}$ values in the dioritic melts. However, since the $\delta^7\text{Li}$ values of our samples show no correlation with indices of crustal assimilation such as LREE/Pb (Ce/Pb, Fig. 10b), upper-crust assimilation had very little effect on the Li isotope values. As the weathered upper crust has small $\delta^7\text{Li}$ values ($\delta^7\text{Li}$ = 0.6 ± 0.6 ‰; Sauzéat *et al.* 2015), upper-crust

contamination will result in decreasing Ce/Pb values with decreasing $\delta^7\text{Li}$. Since our two dioritic samples (09333-1 and 09335-1) have high $\delta^7\text{Li}$ values (+2.36 ‰ and +3.49 ‰) and low Ba/Nb values (52.5 and 47.8), they were the least affected by upper-crustal assimilation and surface processes.

6.c. Oxidation conditions of the magmas

Porphyry copper deposits usually occur in continental-arc settings (Shu *et al.* 2019). Recent research has indicated a close relationship between mineralization and the oxidation state of arc magma, so that Cu–Mo-bearing granitoids indicate oxidized conditions whereas W–Sn deposits indicate more reducing conditions (Ballard *et al.* 2002; Mungall, 2002; Mengason *et al.* 2011). The oxidation state of magma is very important for Cu–Mo mineralization. Experiments show that sulfur mainly exists in the form of S^{6+} and forms a large amount of SO_4^{2-} when $f\text{O}_2$ is high in the system during partial melting. Most sulfur exists in the form of sulfate in magma of over $\Delta\text{FMQ}+1.5$ (Jugo *et al.* 2010). In addition, the solubility of sulfate is over ten times higher than that of sulfide (Sun *et al.* 2015). In the process of partial melting, chalcophile elements such as Cu are incompatible and can enter the melt phase in large quantities (Richards, 2003). High $f\text{O}_2$ can bring massive sulfide during partial melting into the magmatic system to provide material preparation for mineralization. When oxygen fugacity is low during partial melting, S mainly exists as S^{2-} and sulfide solubility is very low. In this case, Cu, Au and Mo will preferentially enter sulfide and it is difficult for them to enter the melt phase. A large quantity of Mesozoic porphyry Cu–Mo deposits have been identified in the eastern CAOB, and the ore-forming rocks associated with fertile Mo deposits are all with high oxidation states ($\text{Ce}^{4+}/\text{Ce}^{3+} > 100$; Shu *et al.* 2019). However, our studied Palaeozoic rocks are not linked to porphyry Cu–Mo deposits, possibly owing to the low to intermediate oxygen fugacity of the magma.

Highly resistant to weathering and alteration, zircon is capable of preserving its physical and chemical characteristics of formation in the deep crust because of its high closure temperature (Hoskin & Schaltegger, 2003); thus, zircon is an ideal mineral for calculating melt oxygen fugacity. The magma $f\text{O}_2$ was calculated after Smythe & Brenan (2016) with the formula:

$$\ln \left[\frac{x_{\text{Ce}^{4+}}^{\text{melt}}}{x_{\text{Ce}^{3+}}^{\text{melt}}} \right] = \frac{1}{4} \ln f\text{O}_2 + \frac{13136(\pm 591)}{T} - 2.064(\pm 0.011) \frac{\text{NBO}}{T} - 8.878(\pm 0.112) \cdot x\text{H}_2\text{O} - 8.955(\pm 0.091)$$

$$\left[\frac{x_{\text{Ce}^{4+}}^{\text{melt}}}{x_{\text{Ce}^{3+}}^{\text{melt}}} \right] = \left[\frac{\sum \text{Ce}_{\text{zircon}} - (\sum \text{Ce}_{\text{melt}} * D_{\text{Ce}^{3+}}^{\text{zircon/melt}})}{\sum \text{Ce}_{\text{melt}} * D_{\text{Ce}^{4+}}^{\text{zircon/melt}} - \sum \text{Ce}_{\text{zircon}}} \right] * 1.04877$$

The partition coefficients of $D_{\text{Ce}^{3+}}^{\text{zircon/melt}}$ and $D_{\text{Ce}^{4+}}^{\text{zircon/melt}}$ were calculated by the lattice strain model (Blundy & Wood, 1994). The NBO/T (the ratio of non-bridging oxygens to tetrahedrally coordinated cations) was calculated following the formula:

$$\text{NBO}/\text{T} = (2\text{A} - 4\sum\text{M}^{\text{IV}}) / \sum\text{M}^{\text{IV}}$$

$\sum\text{M}^{\text{IV}}$ is the number of bridging oxygen bonds in the Si (Al, Ti, P, Fe)–O tetrahedron; A stands for anion, and 2A is the sum of anion bonds (including oxygen ion bonds and effective anion bonds of volatile components); $(2\text{A} - 4\sum\text{M}^{\text{IV}})$ is the number of

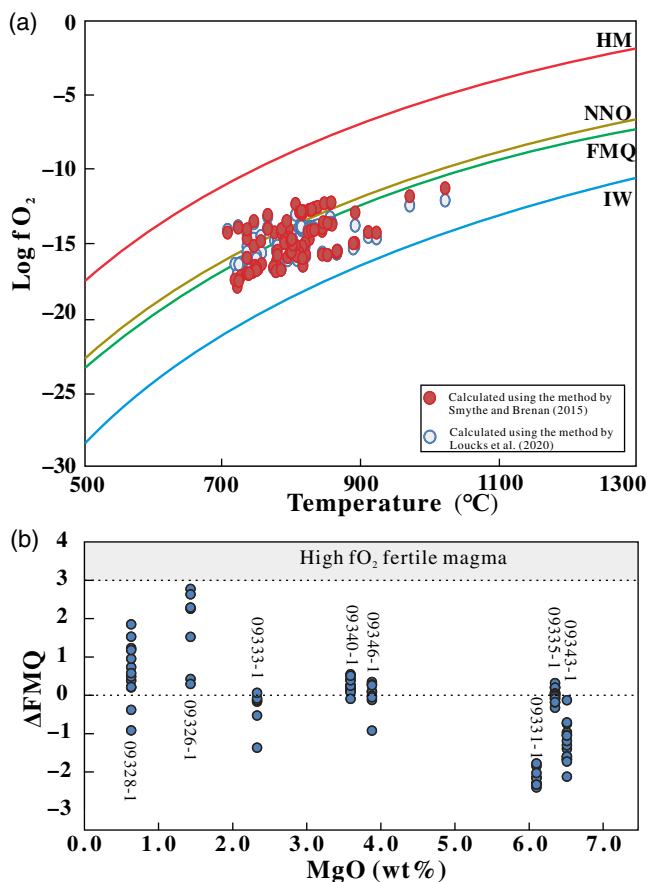


Fig. 12. (Colour online) Zircon oxygen fugacities. (a) Oxygen fugacity versus Ti-in-zircon temperature plot for the Gongzhuling magmatic rocks. The HM, FMQ, NNO and IW buffers are from Myers & Eugster (1983) and O'Neil & Pownceby (1993). (b) Δ FMQ versus MgO plot. Data area for oxidized fertile magma is from Li *et al.* (2019).

non-bridging oxygen bonds in the melt; $(2A - 4\Sigma M^{IV})/\Sigma M^{IV}$ is the number of non-bridging oxygen bonds of each quaternary coordinated cation. The corresponding cation moles (mol) and anion moles (mol) of each component in the melt were obtained by analysing major-element percentage values. Then the molar values $M^{(IV)3+}$ of trivalent cations (Al^{3+} , Fe^{3+}) with tetrahedral coordination were judged: when $\Sigma M^{3+} > \Sigma M^{+} + 2\Sigma M^{2+} + 4Ti$, $M^{(IV)3+} = \Sigma M^{+} + 2\Sigma M^{2+} + 4Ti$; when $\Sigma M^{3+} < \Sigma M^{+} + 2\Sigma M^{2+} + 4Ti$, $M^{(IV)3+} = \Sigma M^{3+}$, where $M^{+} = K + Na + P$ (mol). Molar values of quaternary coordinated cations ΣM^{IV} were calculated by: $\Sigma M^{IV} = Si + P + M^{(IV)3+}$. Anion bond number A was calculated by: $A = O + 1/2(OH + F)$ (Mysen *et al.* 1982).

X_{H_2O} (mole fraction of water dissolved in the melt) of our samples was calculated by means of the thermodynamic method (Nicholls, 1980), combined with the temperature, pressure and f_{H_2O} of magma at the crystallization of zircon. The NBO/T and X_{H_2O} values are listed in online Supplementary Material Table S2.

The absolute oxygen fugacities of the analysed zircons, presented as fO_2 , as well as trace-element concentrations, are listed in online Supplementary Material Table S2. The values of fO_2 were estimated using the zircon/melt Ce anomaly (Ce_N/Ce_N^*) and the zircon Ti thermometer, as in the method described by Smythe & Brennan (2016). The calculated fO_2 values were from FMQ–2.2 to FMQ+2.6 (online Supplementary Material Table S2; Fig. 12a), showing a low to intermediate oxidation state for these magmas.

Also shown for comparison were fO_2 values calculated using the method described by Loucks *et al.* (2020) (online Supplementary Material Table S2; Fig. 12a). Previous research shows that the large porphyry copper deposits in the CAOB are characterized by oxygen fugacity values of early primary magma over Δ FMQ+3.0, which is a common feature of typical arc magmas (Kelley & Cottrell, 2009; Shen *et al.* 2016; Li *et al.* 2019).

The varied fO_2 of each sample may be the results of pretulite ($Sc^{3+} + P^{5+} \rightleftharpoons Zr^{4+} + Si^{4+}$), brabantite ($Ca^{2+} + (U, Th)^{4+} + 2P^{5+} \rightleftharpoons 2Zr^{4+} + 2Si^{4+}$), ximengite-type ($Bi^{3+} + P^{5+} \rightleftharpoons Zr^{4+} + Si^{4+}$) and various REE³⁺–P (e.g. $(Al, Fe)^{3+} + 4(Y, REE)^{3+} + P^{5+} = 4Zr^{4+} + Si^{4+}$) substitution reactions, which generate uneven distributions of trivalent REEs in zircon and large variations of HREEs (Breiter *et al.* 2006; Yang *et al.* 2016). As discussed above, the partition coefficient of $D_{Ce^{3+}}^{zircon/melt}$ was constrained by partition coefficients for other REEs using the lattice strain model (Blundy & Wood, 1994), and these substitution reactions in zircons may cause variations in the values of fO_2 .

The varied low-intermediate redox states (FMQ–2.2 to FMQ+2.6) of the Gongzhuling intermediate–felsic intrusions may imply effects of fractionation crystallization on magma fO_2 . Samples with higher MgO content have lower values of fO_2 (with 09331-1 = Δ FMQ–2.4 ~ Δ FMQ–1.8, 09335-1 = Δ FMQ–0.3 ~ Δ FMQ+0.3, 09343-1 = Δ FMQ–2.1 ~ Δ FMQ–0.1; Fig. 12b). While samples with lower MgO contents have higher values of fO_2 (Fig. 12b). The lattice sites of olivine and clinopyroxene tend to incorporate divalent iron during early fractional crystallization, thus leading to increased concentration of Fe^{3+} in the residual magmatic system (Cottrell & Kelley, 2011). Furthermore, there is a clear positive correlation between the water content and fO_2 in the primary melt, which was recorded by an Fe^{2+} -reduction trend coinciding with decreasing H_2O content in melt inclusions (Kelley & Cottrell, 2012). Our more felsic samples contain a higher water content with higher fO_2 (more hornblende fractionation; online Supplementary Material Table S2), and this is consistent with the above observation.

The samples have undergone minor crustal contamination, which would dramatically change the magma fO_2 , as incorporating reduced crustal materials (e.g. organic carbon) would cause fractionation of primary magnetite, haematite and anhydrite in the magma (Rowins, 2000). However, we did not observe these minerals in our samples. This was also supported by the small variations (up to four ϵ_{Hf} units) in ϵ_{Hf} values of the most mafic sample (09343-1). Furthermore, the δ^7Li values of our samples show no correlation with indices of crustal assimilation such as LREE/Pb (Ce/Pb; Fig. 10b); thus, the upper-crust assimilation had very little effect.

Previous researchers have suggested that the participation of Fe^{3+} -rich oxidized subduction sediments could control the oxidation state of typical continental-arc magmas above the FMQ buffer zone (Mungall, 2002; Kelley & Cottrell, 2009). The reasons for our samples being reduced to moderately oxidized are as following. Firstly, the mantle source was not metasomatized by oxidized sediments, as indicated by the Li isotopes, and modification of the mantle wedge by slab-derived fluids may not indicate a high oxidation state, because the V/Sc-inferred values of fO_2 of the arc magma sources are lower than the FMQ buffer zone, as suggested by Lee *et al.* (2005). Secondly, the mantle source of the Gongzhuling intrusions was metasomatized shortly before partial melting and may have lacked long-time auto-oxidation processes ($3FeO + H_2O = FeO \times Fe_2O_3 + H_2$; Kelley & Cottrell, 2009).

Furthermore, there may lack an intracrustal increase in oxygen fugacity that could be acquired in the lower-crustal source region through the crystal fractionation of minerals which prefer ferrous over ferric iron during fractionation, such as Fe-rich garnet (Tang *et al.* 2018). This is consistent with the absence of large porphyry copper polymetallic deposits in the Gongzhuling area, as porphyry deposits typically form in the thickened arc crust of a continental margin, as was the case for the fertile magma systems of the western CAOB and the Andes (Sillitoe & Thompson, 2010; Shen *et al.* 2016).

6.d. Genetic model and tectonic implications

As discussed above, the middle–late Permian magmatic rocks in southwestern Jilin Province consist of a rock assemblage of dacite tuff, dioritic rocks and biotite syenogranite with SiO₂ contents of 45.7 to 71.9 wt % and calc-alkaline affinities. The above features are similar to those of continental-arc magmatic rocks (Murphy, 2006). The presence of hornblende and biotite indicates that the parental magma was water-rich (Ridolfi *et al.* 2010). Moreover, our samples are all enriched in LILEs and depleted in HFSEs, with positive $\delta^7\text{Li}$ and $\epsilon_{\text{Hf}}(t)$ values. Such geochemical compositions indicate that the source regions have been metasomatized by slab-released fluids shortly before partial melting (Grove *et al.* 2003; Krienitz *et al.* 2012).

The CAOB was formed by the amalgamation and consolidation of multiple terranes as a result of the subduction of the Palaeo-Asian oceanic plate during Palaeozoic time (Xiao *et al.* 2003; Jahn *et al.* 2004), but the timing and location of the terminal closure of the Palaeo-Asian Ocean remain debated (Xiao *et al.* 2003; Wilde, 2015). Zircon U–Pb dating revealed the crystallization ages of the Gongzhuling intermediate–felsic magmatic rocks at 269–258 Ma, which coincides with the ages of a series of Palaeozoic magmatic rocks along the Xra Moron–Changchun Suture Zone. Calc-alkaline I-type granitoids with the same age as the Gongzhuling magmatic rocks are common in the eastern areas of China on both sides of the Xra Moron–Changchun Suture Zone, such as in the Hunchun area, the Liaoyuan Terrane and the Wudaogou and Daheshen regions (Zhang *et al.* 2007, 2014; Yu *et al.* 2008, 2014; Ma *et al.* 2019). This implies that the location of the final closure of the Palaeo-Asian Ocean in NE China occurred along the Xra Moron–Changchun Fault (suture zone), and not the Kaiyuan Fault (Yuan *et al.* 2016). The E–W-striking magmatic belts along both sides of the Solonker–Xra Moron–Changchun Suture Zone probably mark the terminal bidirectional subduction of the Palaeo-Asian oceanic lithosphere, with southwards subduction beneath the North China Block and northwards subduction beneath the amalgamated blocks of NE China (Zhang *et al.* 2014). The subsequent Early Triassic development of high-Sr/Y adakitic magmatic activity within the suture zone is considered to have resulted from crustal thickening caused by the amalgamation of the North China Block and the combined NE China blocks (Cao *et al.* 2013). In addition, metamorphism of the Hulan Group at *c.* 250 Ma was related to the amalgamation of the North China Block and the combined NE China blocks along the Solonker–Xra Moron–Changchun Suture Zone, providing further evidence for the timing of the final closure of the Palaeo-Asian Ocean (Wu *et al.* 2007).

Our samples, together with the aforementioned magmatic rocks that crop out along the Xra Moron–Changchun Suture Zone, indicate that Andean-type magmatism was still active during

middle–late Permian time, but the lack of deep-marine Triassic sediments within the eastern CAOB precludes the closure of the Palaeo-Asian Ocean as being as late as the Triassic Period (JBGMR, 1988; Xiao *et al.* 2003). Therefore, the middle–late Permian Gongzhuling dacite tuff and intermediate–felsic intrusive rocks may represent the final stage of arc magmatism (269–258 Ma) in response to the southward subduction of the Palaeo-Asian oceanic plate beneath the North China Block.

6.e. Constraints on basement compositions and crustal growth of the Liaoyuan Accretionary Belt

The Liaoyuan Accretionary Belt (Liaoyuan Terrane) is separated from the northern margin of the North China Craton by the E–W-trending Kaiyuan Fault (the northern margin fault of the North China Craton). It was considered the eastern extension of the Bainaimiao arc belt, but Nd–Hf isotopic compositions of early Palaeozoic arc-related magmatic rocks show that its basement compositions are very different from the western part of the Bainaimiao arc belt (Zhang *et al.* 2014). Recently, a Mesoproterozoic granitoid pluton with a zircon U–Pb age of *c.* 1.40 Ga has been identified from the Liaoyuan Accretionary Belt, indicating the existence of Precambrian microcontinental fragments in this area (Li *et al.* 2021). The *c.* 1.40 Ga granitoids exhibit positive $\epsilon_{\text{Hf}}(t)$ values of +3.31 to +11.1 and old two-stage model ages ($T_{\text{DM}2}$) of 1480 Ma to 2128 Ma, indicating the existence of some Palaeoproterozoic crustal materials beneath the Liaoyuan Accretionary Belt.

Our new zircon Hf isotopic analytical results of continental-arc-related dacite tuffs and intermediate–felsic intrusions including those emplaced into the *c.* 1.40 Ga granitoids in the Liaoyuan Accretionary Belt show that all these Permian magmatic rocks are characterized by high positive zircon $\epsilon_{\text{Hf}}(t)$ values of +0.7 to +13.1 and young Hf $T_{\text{DM}2}$ model ages of 1.2–0.46 Ga. The above zircon Hf isotopic compositions are similar to those of the late Palaeozoic – early Mesozoic intrusive rocks in middle Jilin Province with $\epsilon_{\text{Hf}}(t)$ of +0.23 ~ +10.37 and Neoproterozoic Hf model ages (Cao *et al.* 2013). These Hf isotopic compositions indicate that although some Palaeoproterozoic crustal materials exist beneath the Liaoyuan Accretionary Belt as suggested by the *c.* 1.40 Ga granitoids, the Palaeoproterozoic crustal materials are rare in the Liaoyuan Accretionary Belt and its crustal growth occurred mainly during the Neoproterozoic period.

7. Conclusions

- (1) The middle–late Permian intermediate intrusive rocks in the Gongzhuling area of NE China were formed by the mixing of mantle-derived mafic magmas and lower-crust-derived felsic magmas. The biotite syenogranite in the Gongzhuling area was formed by partial melting of the underplated arc basalt of Neoproterozoic age.
- (2) The mantle source was isotopically depleted, as revealed by highly positive $\epsilon_{\text{Hf}}(t)$ values (+0.7 to +13.1), and it had been metasomatized by Li-rich fluids released from subducted oceanic crust.
- (3) The low-intermediate oxidation states revealed by zircon trace-element concentrations suggest a relatively reduced source for these continental-arc magmas, lacking a lower-crust increase in $f\text{O}_2$ acquired through fractionation of high-pressure minerals.

- (4) The positive zircon $\epsilon_{\text{Hf}}(t)$ values (+0.7 to +13.1) and young Hf T_{DM2} model ages (1.2–0.46 Ga) of the Permian granitoids indicate that the Palaeoproterozoic crustal materials are rare in the Liaoyuan Accretionary Belt and its crustal growth occurred mainly during the Neoproterozoic period.

Supplementary material. To view supplementary material for this article, please visit <https://doi.org/10.1017/S0016756822000711>

Acknowledgements. This work was supported by the National Natural Science Foundation of China (41725011, 41920104004), the National Key Research and Development Programme of China (2018YFC0603802) and the Science and Technology Foundation of the Guangxi Province (2018GXNSFAA138063). We thank Y. L. Xiao, Z. C. Hu, K. J. Hou and H. Li for technical support during the Li isotope, LA-ICP-MS U–Pb, *in situ* Lu–Hf and major- and trace-element analytical work.

Funding. National Natural Science Foundation of China, Grant/Award Number: 41725011, 41920104004; National Key Research and Development Programme of China, Grant/Award Number: 2018YFC0603802; Science and Technology Foundation of the Guangxi Province Award Number: 2018GXNSFAA138063. Authors' contributions: Chang-Jian Chen and Shuan-Hong Zhang designed this study and wrote the manuscript.

Conflicts of interest. None.

References

- Andersen T (2002) Correction of common lead in U–Pb analyses that do not report ^{204}Pb . *Chemical Geology* **192**, 59–79.
- Armienti P and Gasperini D (2007) Do we really need mantle components to define mantle composition? *Journal of Petrology* **48**, 693–709.
- Ballard JR, Palin MJ and Campbell IH (2002) Relative oxidation states of magmas inferred from Ce(IV)/Ce(III) in zircon: application to porphyry copper deposits of northern Chile. *Contributions to Mineralogy and Petrology* **144**, 347–64.
- Berger G, Schott J and Guy C (1988) Behavior of Li, Rb and Cs during basalt glass and olivine dissolution and chlorite, smectite and zeolite precipitation from seawater: experimental investigations and modelization between 50° and 300°C. *Chemical Geology* **71**, 297–312.
- Blevin PL and Chappell BW (1992) The role of magma sources, oxidation states and fractionation in determining the granite metallogeny of eastern Australia. *Transactions of the Royal Society of Edinburgh: Earth Sciences* **83**, 305–16.
- Blundy J and Wood B (1994) Prediction of crystal-melt partition coefficients from elastic moduli. *Nature* **2**, 63–114.
- Bourdon E, Eissen J-P, Monzier M, Robin C, Martin H, Cotton J and Hall ML (2002) Adakite-like lavas from Antisana volcano (Ecuador): evidence for slab melt metasomatism beneath the Andean Northern Volcanic Zone. *Journal of Petrology* **43**, 199–217.
- Boynnton WV (1984) Chapter 3 – Cosmochemistry of the rare earth elements: meteorite studies. *Developments in Geochemistry* **2**, 63–114.
- Breiter K, Förster H-J and Škoda R (2006) Extreme P-, Bi-, Nb-, Sc-, U- and F-rich zircon from fractionated perphosphorous granites: the peraluminous Podlesi granite system, Czech Republic. *Lithos* **88**, 15–34.
- Bryant CJ, Chappell BW, Bennett VC and McCulloch MT (2004) Lithium isotopic compositions of the New England Batholith: correlations with inferred source rock compositions. *Transactions of the Royal Society of Edinburgh: Earth Sciences* **95**, 199–214.
- Cahalan RC, Kelly ED and Carlson WD (2014) Rates of Li diffusion in garnet: coupled transport of Li and Y+REEs. *American Mineralogist* **99**, 1676–82.
- Cao HH, Xu WL, Pei FP, Wang ZW, Wang F and Wang ZJ (2013) Zircon U–Pb geochronology and petrogenesis of the Late Paleozoic–Early Mesozoic intrusive rocks in the eastern segment of the northern margin of the North China Block. *Lithos* **170**, 191–207.
- Chan LH, Alt JC and Teagle DAH (2002) Lithium and lithium isotope profiles through the upper oceanic crust: a study of seawater–basalt exchange at ODP Sites 504B and 896A. *Earth and Planetary Science Letters* **201**, 187–201.
- Chan LH and Edmond JM (1988) Variation of lithium isotope composition in the marine environment: a preliminary report. *Geochimica et Cosmochimica Acta* **52**, 1711–17.
- Chan LH, Edmond JM, Thompson G and Gillis K (1992) Lithium isotopic composition of submarine basalts: implications for the lithium cycle in the oceans. *Earth and Planetary Science Letters* **108**, 151–60.
- Chan LH and Kastner M (2000) Lithium isotopic compositions of pore fluids and sediments in the Costa Rica subduction zone: implications for fluid processes and sediment contribution to the arc volcanoes. *Earth and Planetary Science Letters* **183**, 275–90.
- Chen B and Arakawa Y (2005) Elemental and Nd–Sr isotopic geochemistry of granitoids from the West Junggar foldbelt (NW China), with implications for Phanerozoic continental growth. *Geochimica et Cosmochimica Acta* **69**, 1307–20.
- Chen B, Gu HO, Chen Y, Sun KK and Chen W (2018) Lithium isotope behaviour during partial melting of metapelites from the Jiangnan Orogen, South China: implications for the origin of REE tetrad effect of F-rich granite and associated rare-metal mineralization. *Chemical Geology* **483**, 372–84.
- Chen B, Jahn BM and Tian W (2009) Evolution of the Solonker suture zone: constraints from zircon U–Pb ages, Hf isotopic ratios and whole-rock Nd–Sr isotope compositions of subduction- and collision-related magmas and fore-arc sediments. *Journal of Asian Earth Sciences* **34**, 245–57.
- Claeson DT and Meurer WP (2004) Fractional crystallization of hydrous basaltic “arc-type” magmas and the formation of amphibole-bearing gabbroic cumulates. *Contributions to Mineralogy and Petrology* **147**, 288–304.
- Cottrell E and Kelley KA (2011) The oxidation state of Fe in MORB glasses and the oxygen fugacity of the upper mantle. *Earth and Planetary Science Letters* **305**, 270–82.
- Dohmen R, Kasemann SA, Coogan L and Chakraborty S (2010) Diffusion of Li in olivine. Part I: experimental observations and a multi species diffusion model. *Geochimica et Cosmochimica Acta* **74**, 274–92.
- Eizenhöfer PR, Zhao G, Zhang J and Sun M (2014) Final closure of the Paleo-Asian Ocean along the Solonker Suture Zone: constraints from geochronological and geochemical data of Permian volcanic and sedimentary rocks. *Tectonics* **33**, 441–63.
- Elliott T, Jeffcoate A and Bouman C (2004) The terrestrial Li isotope cycle: light-weight constraints on mantle convection. *Earth and Planetary Science Letters* **220**, 231–45.
- Feng GY, Liu S, Zhong H, Jia DC, Qi YQ, Wang T and Yang YH (2010) Geochemical characteristics and petrogenesis of late Paleozoic mafic rocks from Yumuchuan, Jilin Province. *Geochimical* **39**, 427–38 (in Chinese with English abstract).
- Flesch GD, Anderson Jr AR and Svec HJ (1973) A secondary isotopic standard for $^6\text{Li}/^7\text{Li}$ determinations. *International Journal of Mass Spectrometry and Ion Physics* **12**, 265–72.
- Gao Y and Casey JF (2012) Lithium isotope composition of ultramafic geological reference materials JP-1 and DTS-2. *Geostandards and Geoanalytical Research* **36**, 75–81.
- Gerdes A, Wörner G and Finger F (2000) Hybrids, magma mixing and enriched mantle melts in post-collisional Variscan granitoids: the Rastenbergl Pluton, Austria. In *Orogenic Processes: Quantification and Modelling in the Variscan Belt* (eds W Franke, V Haak, O Oncken and D Tanner), pp. 415–31. Geological Society of London, Special Publication no. 179.
- Grove TL, Elkins-Tanton LT, Parman SW, Chatterjee N, Müntener O and Gaetani GA (2003) Fractional crystallization and mantle-melting controls on calc-alkaline differentiation trends. *Contributions to Mineralogy and Petrology* **145**, 515–33.
- Guo F, Li HX, Fan WM, Li JY, Zhao L and Huang MW (2015) Variable sediment flux in generation of Permian subduction-related mafic intrusions from the Yanbian region, NE China. *Lithos* **261**, 195–215.
- Halama R, John T, Herms P, Hauff F and Schenk V (2011) A stable (Li, O) and radiogenic (Sr, Nd) isotope perspective on metasomatic processes in a subducting slab. *Chemical Geology* **281**, 151–66.
- Hawkesworth CJ, Hergt JM, Ellam RM and McDermott F (1991) Element fluxes associated with subduction-related magmatism. *Philosophical*

- Transactions of the Royal Society of London Series A—Mathematical Physical and Engineering Sciences* **335**, 393–405.
- Hoskin PWO and Schaltegger U** (2003) The composition of zircon and igneous and metamorphic petrogenesis. *Reviews in Mineralogy and Geochemistry* **53**, 27–62.
- Jackson SE, Pearson NJ, Griffin WL and Belousova EA** (2004) The application of laser ablation-inductively coupled plasma-mass spectrometry to in situ U–Pb zircon geochronology. *Chemical Geology* **211**, 47–69.
- Jahn BM** (2000) Massive granitoid generation in central Asia: Nd isotopic evidence and implication for continental growth in the Phanerozoic. *Episodes* **23**, 82–92.
- Jahn BM, Capdevila R, Liu D, Vernon A and Badarch G** (2004) Sources of Phanerozoic granitoids in the transect Bayanhongor–Ulaan Baatar, Mongolia: geochemical and Nd isotopic evidence, and implications for Phanerozoic crustal growth. *Journal of Asian Earth Sciences* **23**, 629–53.
- Jahn BM, Wu FY, Capdevila R, Martineau F, Zhao Z and Wang Y** (2001) Highly evolved juvenile granites with tetrad REE patterns: the Woduhe and Baerzhe granites from the great Xing'an mountains in NE China. *Lithos* **59**, 171–98.
- Janoušek V and Moya J-F** (2020) Whole-rock geochemical modelling of granite genesis: the current state of play. In *Post-Archean Granitic Rocks: Petrogenetic Processes and Tectonic Environments* (eds V Janoušek, B Bonin, WJ Collins, F Farina and P Bowden), pp. 267–91. Geological Society of London, Special Publication no. 491.
- JBGMR (Jilin Bureau of Geology and Mineral Resources)** (1988) *Regional Geology of Jilin Province*. Beijing: Geological Publishing House, pp. 301–85 (in Chinese with English summary).
- Jeffcoate AB, Elliott T, Kasemann SA, Ionov D, Cooper K and Brooker R** (2007) Li isotope fractionation in peridotites and mafic melts. *Geochimica et Cosmochimica Acta* **71**, 202–18.
- Jian P, Liu D, Kroner A, Windley BF, Shi Y, Zhang W, Zhang F, Miao L, Zhang L and Tomurhuu D** (2010) Evolution of a Permian intraoceanic arc–trench system in the Solonker suture zone, Central Asian Orogenic Belt, China and Mongolia. *Lithos* **118**, 169–90.
- John T, Gussone N, Podladchikov Y, Bebout GE, Dohmen R, Halama R, Klemm R, Magna T and Seitz H-M** (2012) Volcanic arcs fed by rapid pulsed fluid flow through subducting slabs. *Nature Geoscience* **5**, 489–92.
- Jugo PJ, Wilke M and Botcharnikov RE** (2010) Sulfur K-edge XANES analysis of natural and synthetic basaltic glasses: implications for S speciation and S content as function of oxygen fugacity. *Geochimica et Cosmochimica Acta* **74**, 5926–38.
- Kelley KA and Cottrell E** (2009) Water and the oxidation state of subduction zone magmas. *Science* **325**, 605–7.
- Kelley KA and Cottrell E** (2012) The influence of magmatic differentiation on the oxidation state of Fe in a basaltic arc magma. *Earth and Planetary Science Letters* **329–330**, 109–21.
- Kemp AIS, Hawkesworth CJ, Paterson BA and Kinny PD** (2006) Episodic growth of the Gondwana supercontinent from hafnium and oxygen isotopes in zircon. *Nature* **439**, 580–3.
- Kirkland CL, Smithies RH, Taylor RJM, Evans N and McDonald B** (2015) Zircon Th/U ratios in magmatic environs. *Lithos* **212–215**, 397–414.
- Kovalenko VI, Yarmolyuk VV, Kovach VP, Kotov AB and Larin AM** (2004) Isotope provinces, mechanisms of generation and sources of the continental crust in the Central Asian mobile belt: geological and isotopic evidence. *Journal of Asian Earth Sciences* **23**, 605–27.
- Krienitz MS, Garbe-Schonberg CD, Romer RL, Meixner A, Haase KM and Stronck NA** (2012) Lithium isotope variations in ocean island basalts—implications for the development of mantle heterogeneity. *Journal of Petrology* **53**, 2333–47.
- Lee CTA, Leeman WP, Canil D and Li ZXA** (2005) Similar V/Sc systematics in MORBs and arc basalts: implications for the oxygen fugacities of their mantle source regions. *Journal of Petrology* **46**, 2313–36.
- Li HX, Guo F, Li CW and Zhao L** (2010) Late Paleozoic subduction of the Paleo-Asian Ocean: geochronological and geochemical records from Qianshan mafic intrusion in Hunchun area, NE China. *Acta Petrologica Sinica* **26**, 1530–40.
- Li CH, Liu ZH, Dong X, Xu Z, Wen K, Wang S, Wang C and Gao Y** (2021) Mesoproterozoic (~1.4 Ga) magmatism in the Liaoyuan Accretionary Belt, NE China: new implications for tectonic affinity and crustal evolution of microcontinents along the southern Central Asian Orogenic Belt. *Precambrian Research* **365**, 106389. doi: [10.1016/j.precamres.2021.106389](https://doi.org/10.1016/j.precamres.2021.106389).
- Li WK, Yang ZM, Cao K, Lu YJ and Sun MY** (2019) Redox-controlled generation of the giant porphyry Cu–Au deposit at Pulang, southwest China. *Contributions to Mineralogy and Petrology* **174**, 1–34.
- Liu YS, Hu ZC, Gao S, Günther D, Xu J, Gao CG and Chen HH** (2008) In situ analysis of major and trace elements of anhydrous minerals by LA-ICP-MS without applying an internal standard. *Chemical Geology* **257**, 34–43.
- Liu YS, Hu ZC, Zong KQ, Gao CG, Gao S, Xu J and Chen HH** (2010) Reappraisal and refinement of zircon U–Pb isotope and trace element analyses by LA-ICP-MS. *Chinese Science Bulletin* **55**, 1535–46.
- Liu YJ, Li WM, Feng ZQ, Wen QB, Neubauer F and Liang CY** (2017) A review of the Paleozoic tectonics in the eastern part of Central Asian Orogenic Belt. *Gondwana Research* **43**, 123–48.
- Loucks RR, Fiorentini ML and Henriquez GL** (2020) New magmatic oxybarometer using trace elements in zircon. *Journal of Petrology* **61**, ega034. doi: [10.1093/petrology/egaa034](https://doi.org/10.1093/petrology/egaa034).
- Ludwig KR** (2003) User's Manual for Isoplot 3.00: A Geochronological Toolkit for Microsoft Excel. Berkeley Geochronology Center, Special Publication no. 4.
- Ma XH, Chen CJ, Zhao JX, Qiao SL and Zhou ZH** (2019) Late Permian intermediate and felsic intrusions in the eastern Central Asian Orogenic Belt: final-stage magmatic record of Paleo-Asian Oceanic subduction? *Lithos* **326–327**, 265–78.
- Ma HT, Ma X, Chen JF, Chen B, Li C, Zhou LM and Yang HZ** (2020) The Zhangjiatun igneous complex in the southeastern margin of the Central Asian Orogenic Belt, NE China: evidence for an Early Paleozoic intraoceanic arc. *Journal of Asian Earth Sciences* **194**, 104182. doi: [10.1016/j.jseas.2019.104182](https://doi.org/10.1016/j.jseas.2019.104182).
- Magna T, Janoušek V, Kohút M, Oberli F and Wiechert U** (2010) Fingerprinting sources of orogenic plutonic rocks from Variscan belt with lithium isotopes and possible link to subduction-related origin of some A-type granites. *Chemical Geology* **274**, 94–107.
- Magna T, Novak M, Cempirek J, Janoušek V, Ullmann CV and Wiechert U** (2016) Crystallographic control on lithium isotope fractionation in Archean to Cenozoic lithium–cesium–tantalum pegmatites. *Geology* **44**, 655–8.
- Magna T, Wiechert U, Grove TL and Halliday AN** (2006) Lithium isotope fractionation in the southern Cascadia subduction zone. *Earth and Planetary Science Letters* **250**, 428–43.
- Marks MAW, Rudnick RL, McCammon C, Vennemann T and Markl G** (2007) Arrested kinetic Li isotope fractionation at the margin of the Ilimaussaq complex, South Greenland: evidence for open-system processes during final cooling of peralkaline igneous rocks. *Chemical Geology* **246**, 207–30.
- Marschall HR, Pogge von Strandmann PAE, Seitz HM, Elliot T and Niu YL** (2007) The lithium isotopic composition of orogenic eclogites and deep subducted slabs. *Earth and Planetary Science Letters* **262**, 563–80.
- Mengason MJ, Candela PA and Piccoli PM** (2011) Molybdenum, tungsten and manganese partitioning in the system pyrrhotite–FeSO melt–rhyolite melt: impact of sulfide segregation on arc magma evolution. *Geochimica et Cosmochimica Acta* **75**, 7018–30.
- Miller DM, Goldstein SL and Langmuir CH** (1994) Cerium/lead and lead isotope ratios in arc magmas and the enrichment of lead in the continents. *Nature* **368**, 514–20.
- Moriguti T and Nakamura E** (1998) High-yield lithium separation and the precise isotopic analysis for natural rock and aqueous samples. *Chemical Geology* **145**, 91–104.
- Mungall JE** (2002) Roasting the mantle: slab melting and the genesis of major Au and Au-rich Cu deposits. *Geology* **30**, 915–8.
- Murphy JB** (2006) Arc magmatism I: relationship between tectonic evolution and petrogenesis. *Geoscience Canada* **33**, 145–216.
- Myers J and Eugster HP** (1983) The system FeSO: oxygen buffer calibrations to 1500K. *Contributions to Mineralogy and Petrology* **82**, 75–90.

- Mysen BO, Virgo D and Seifert FA** (1982) The structure of silicate melts: implications for chemical and physical properties of natural magma. *Reviews of Geophysics and Space Physics* **20**, 353–83.
- Nicholls J** (1980) A simple thermodynamic model for estimating the solubility of H₂O in magmas. *Contributions to Mineralogy and Petrology* **74**, 211–20.
- Nishio Y, Nakai S, Ishii T and Sano Y** (2007) Isotopic systematics of Li, Sr, Nd and volatiles in Indian Ocean MORBs of the Rodrigues Triple Junction: constraints on the origin of DUPAL anomaly. *Geochimica et Cosmochimica Acta* **71**, 745–59.
- Nozaka T and Liu Y** (2002) Petrology of the Hegenshan ophiolite and its implications for the tectonic evolution of northern China. *Earth and Planetary Science Letters* **202**, 89–104.
- O'Neil HSC and Pownceby MI** (1993) Thermodynamic data from redox reactions at high temperatures. I. An experimental and theoretical assessment of the electrochemical method using stabilized zirconia electrolytes with revised values for the Fe–FeO, Co–CoO, Ni–NiO and Cu–Cu₂O oxygen buffers, and new data for the W–WO₂ buffer. *Contributions to Mineralogy and Petrology* **114**, 296–314.
- Parkinson IJ, Hammond SJ, James RH and Rogers NW** (2007) High-temperature lithium isotope fractionation: insights from lithium isotope diffusion in magmatic systems. *Earth and Planetary Science Letters* **257**, 609–21.
- Pearce JA, Baker PE, Harvey PK and Luff IW** (1995) Geochemical evidence for subduction fluxes, mantle melting and fractional crystallization beneath the south Sandwich Island Arc. *Journal of Petrology* **36**, 1073–109.
- Penniston-Dorland SC, Bebout GE, Pogge von Strandmann PAE, Elliott T and Sorensen SS** (2012) Lithium and its isotopes as tracers of subduction zone fluids and metasomatic processes: evidence from the Catalina Schist, California, USA. *Geochimica et Cosmochimica Acta* **77**, 530–45.
- Petford N and Gallagher K** (2001) Partial melting mafic (amphibolitic) lower crust by periodic influx of basaltic magma. *Earth and Planetary Science Letters* **193**, 483–99.
- Pupin JP** (1980) Zircon and granite petrology. *Contributions to Mineralogy and Petrology* **73**, 207–20.
- Qiu L, Rudnick RL, McDonough WF and Bea F** (2011) The behavior of lithium in amphibolite-to granulite-facies rocks of the Ivrea-Verbanese Zone, NW Italy. *Chemical Geology* **289**, 76–85.
- Rapp RP and Watson EB** (1995) Dehydration melting of metabasalt at 8–32 kbar: implications for continental growth and crust-mantle recycling. *Journal of Petrology* **36**, 891–931.
- Richards JP** (2003) Tectono-magmatic precursors for porphyry Cu (Mo–Au) deposit formation. *Economic Geology* **98**, 1515–33.
- Richter FM, Davis AM, Depaolo DJ and Watson EB** (2003) Isotope fractionation by chemical diffusion between molten basalt and rhyolite. *Geochimica et Cosmochimica Acta* **67**, 3905–23.
- Ridolfi F, Renzulli A and Puerini M** (2010) Stability and chemical equilibrium of amphibole in calc-alkaline magmas: an overview, new thermobarometric formulations and application to subduction-related volcanoes. *Contributions to Mineralogy and Petrology* **160**, 45–66.
- Rollinson H** (1993) *Using Geochemical Data: Evaluation, Presentation, Interpretation*. London: Longman Scientific and Technical, pp. 108–11.
- Romer RL, Meixner A and Forster HJ** (2014) Lithium and boron in late-orogenic granites – isotopic fingerprints for the source of crustal melts? *Geochimica et Cosmochimica Acta* **131**, 98–114.
- Rowins SM** (2000) Reduced porphyry copper–gold deposits: a new variation on an old theme. *Geology* **28**, 491–4.
- Rudnick RL and Gao S** (2014) Composition of the continental crust. In *Treatise on Geochemistry, Second Edition, Volume 4* (eds HD Holland and KK Turekian), pp. 1–51. Oxford: Elsevier-Perigamon.
- Rudnick RL, Tomascak PB, Njo HB and Gardner LR** (2004) Extreme lithium isotopic fractionation during continental weathering revealed in saprolites from South Carolina. *Chemical Geology* **212**, 45–57.
- Ruzhentsev SV and Pospelov II** (1992) The South Mongolian Variscan Fold System. *Geotectonics* **26**, 383–95.
- Ryan JG and Langmuir CH** (1987) The systematics of lithium abundances in young volcanic rocks. *Geochimica et Cosmochimica Acta* **51**, 1727–41.
- Sartbaeva A, Wells SA and Redfern SAT** (2004) Li⁺ ion motion in quartz and β-eucryptite studied by dielectric spectroscopy and atomistic simulations. *Journal of Physics: Condensed Matter* **16**, 8173. doi: [10.1088/0953-8984/16/46/005](https://doi.org/10.1088/0953-8984/16/46/005).
- Sauzéat L, Rudnick RL, Chauvel C, Garçon M and Tang M** (2015) New perspectives on the Li isotopic composition of the upper continental crust and its weathering signature. *Earth and Planetary Science Letters* **428**, 181–92.
- Shao JA and Tang KD** (1995) *Terranes in Northeast China and Evolution of Northeast Asia Continental Margin*. Beijing: Seismic Press, pp. 1–209 (in Chinese).
- Shen P, Hattori K, Pan H, Jackson S and Seitmuratova E** (2016) Oxidation condition and metal fertility of granitic magmas: zircon trace-element data from porphyry Cu deposits in the Central Asian Orogenic belt. *Economic Geology* **110**, 1861–78.
- Shu QH, Chang ZS, Lai Y, Hu X, Wu H, Zhang Y, Wang P, Zhai D and Zhang C** (2019) Zircon trace elements and magma fertility: insights from porphyry (-skarn) Mo deposits in NE China. *Mineral Deposita* **54**, 645–56.
- Sillitoe RH and Thompson JFH** (2010) Intrusion-related vein gold deposits: types, tectono-magmatic settings and difficulties of distinction from orogenic gold deposits. *Resource Geology* **48**, 237–50.
- Simons KK, Harlow GE, Brueckner HK, Goldstein SL, Sorensen SS and Hemming NG** (2010) Lithium isotopes in Guatemalan and Franciscan HP–LT rocks: insights into the role of sediment-derived fluids during subduction. *Geochimica et Cosmochimica Acta* **74**, 3621–41.
- Sisson TW and Grove TL** (1993) Experimental investigations of the role of water in calc-alkaline differentiation and subduction zone magmatism. *Contributions to Mineralogy and Petrology* **113**, 143–66.
- Smythe DJ and Brenan JM** (2016) Magmatic oxygen fugacity estimated using zircon–melt partitioning of cerium. *Earth and Planetary Science Letters* **453**, 260–6.
- Sun H, Gao YJ, Xiao YL, Gu HO and Casey JF** (2016) Lithium isotope fractionation during incongruent melting: constraints from post-collisional leucogranite and residual enclaves from Bengbu Uplift, China. *Chemical Geology* **439**, 71–82.
- Sun WD, Huang RF, Li H, Hu Y-B, Zhang C-C, Sun S-J, Zhang L-P, Ding X, Li C-Y, Zartman RE and Ling M-X** (2015) Porphyry deposits and oxidized magmas. *Ore Geology Reviews* **65**, 97–131.
- Sun SS and McDonough W** (1989) Chemical and isotopic systematics of oceanic basalts: implications for mantle composition and processes. In *Magmatism in the Ocean Basins* (eds AD Saunders and MJ Norry), pp. 313–45. Geological Society of London, Special Publication no. 42.
- Sun CY, Tang J, Xu WL, Li Y and Zhao S** (2017) Crustal accretion and reworking processes of micro-continental massifs within orogenic belt: a case study of the Erguna Massif, NE China. *Science China Earth Sciences* **60**, 1256–67.
- Tang M, Erdman M, Eldridge G and Lee CT** (2018) The redox “filter” beneath magmatic orogens and the formation of continental crust. *Science Advances* **4**, eaar4444. doi: [10.1126/sciadv.aar4444](https://doi.org/10.1126/sciadv.aar4444).
- Teng F-Z, McDonough WF, Rudnick RL, Dalpé C, Tomascak PB, Chappell BW and Gao S** (2004) Lithium isotopic composition and concentration of the upper continental crust. *Geochimica et Cosmochimica Acta* **68**, 4167–78.
- Teng FZ, McDonough WF, Rudnick RL and Walker RJ** (2006) Diffusion-driven extreme lithium isotopic fractionation in country rocks of the Tin Mountain pegmatite. *Earth and Planetary Science Letters* **243**, 701–10.
- Teng FZ, McDonough WF, Rudnick RL and Wing BA** (2007) Limited lithium isotopic fractionation during progressive metamorphic dehydration in metapelites: a case study from the Onawa contact aureole, Maine. *Chemical Geology* **239**, 1–12.
- Teng F-Z, Rudnick RL, McDonough WF, Gao S, Tomascak PB and Liu YS** (2008) Lithium isotopic composition and concentration of the deep continental crust. *Chemical Geology* **255**, 47–59.
- Teng FZ, Rudnick RL, McDonough WF and Wuc FY** (2009) Lithium isotopic systematics of A-type granites and their mafic enclaves: further constraints on the Li isotopic composition of the continental crust. *Chemical Geology* **262**, 370–9.
- Thirlwall MF, Smith TE, Graham AM, Theodorou N, Hollings P, Davidson JP and Arculus RJ** (1994) High field strength element anomalies in arc lavas: source or process? *Journal of Petrology* **35**, 819–38.

- Tian SH, Hou Z, Tian Y, Zhao Y, Hou K, Li X, Zhang Y, Hu W, Mo X and Yang ZJ (2018) Lithium content and isotopic composition of the juvenile lower crust in southern Tibet. *Gondwana Research* **62**, 198–211.
- Tomascak PB, Tera F, Helz RT and Walker RJ (1999) The absence of lithium isotope fractionation during basalt differentiation: new measurements by multicollector sector ICP-MS. *Geochimica et Cosmochimica Acta* **63**, 907–10.
- Vigier N, Decarreau A, Millot R, Carignan J, Petit S and France-Lanord C (2008) Quantifying Li isotope fractionation during smectite formation and implications for the Li cycle. *Geochimica et Cosmochimica Acta* **72**, 780–92.
- Wang HZ and Mo XX (1995) An outline of the tectonic evolution of China. *Episodes* **18**, 6–16.
- Wang T, Tong Y, Zhang L, Li S, Huang H, Zhang JJ, Guo L, Yang QD, Hong DW, Donskaya T, Gladkochub D and Tserendash N (2017) Phanerozoic granitoids in the central and eastern parts of Central Asia and their tectonic significance. *Journal of Asian Earth Sciences* **145**, 368–92.
- Wang ZJ, Xu WL, Pei FP, Wang ZW and Li Y (2015a) Geochronology and provenance of detrital zircons from late Palaeozoic strata of central Jilin Province, Northeast China: implications for the tectonic evolution of the eastern Central Asian Orogenic Belt. *International Geology Review* **57**, 211–28.
- Wang ZJ, Xu WL, Pei FP, Wang ZW, Li Y and Cao HH (2015b) Geochronology and geochemistry of middle Permian–Middle Triassic intrusive rocks from central–eastern Jilin Province, NE China: constraints on the tectonic evolution of the eastern segment of the Paleo-Asian Ocean. *Lithos* **238**, 13–25.
- Wilde SA (2015) Final amalgamation of the Central Asian Orogenic Belt in NE China: Paleo-Asian Ocean closure versus Paleo-Pacific plate subduction – a review of the evidence. *Tectonophysics* **662**, 345–62.
- Wu FY, Jahn BM, Wilde S and Sun DY (2000) Phanerozoic crustal growth: U–Pb and Sr–Nd isotopic evidence from the granites in northeastern China. *Tectonophysics* **328**, 89–113.
- Wu FY, Sun DY, Ge WC, Zhang YB, Grant ML, Wilde SA and Jahn BM (2011) Geochronology of the Phanerozoic granitoids in northeastern China. *Journal of Asian Earth Sciences* **41**, 1–30.
- Wu FY, Yang YH, Xie LW, Yang JH and Xu P (2006) Hf isotopic compositions of the standard zircons and baddeleyites used in U–Pb geochronology. *Chemical Geology* **234**, 105–26.
- Wu FY, Zhao GC, Sun DY, Wilde SA and Yang JH (2007) The Heilongjiang Group: a Jurassic accretionary complex in the Jiamusi Massif at the western Pacific margin of northeastern China. *Island Arc* **16**, 156–72.
- Wunder B, Meixner A, Romer RL and Heinrich W (2006) Temperature-dependent isotopic fractionation of lithium between clinopyroxene and high-pressure hydrous fluids. *Contributions to Mineralogy and Petrology* **151**, 112–20.
- Xiao WJ, Windley BF, Hao J and Zhai MG (2003) Accretion leading to collision and the Permian Solonker suture, Inner Mongolia, China: termination of the central Asian orogenic belt. *Tectonics* **22**, 8–20.
- Xiao WJ, Windley B, Huang BC, Han CM, Yuan C, Chen HL, Sun M, Sun S and Li JL (2009) End-Permian to mid-Triassic termination of the accretionary processes of the southern Altaids: implications for the geodynamic evolution, Phanerozoic continental growth and metallogeny of Central Asia. *International Journal of Earth Sciences* **98**, 1189–217.
- Xin YL, Ren JL, Peng YJ and Sun XQ (2011) Ending of the mountain-building movement of Xing'an-Mongolian-Ji-Hei orogenic belt in northeast China: evidence from Late Triassic molasse (geotectonic phase). *Geology and Resources* **20**, 413–19 (in Chinese with English abstract).
- Xu WL, Pei FP, Wang F, Meng E, Ji WQ, Yang DB and Wang W (2013) Spatial-temporal relationships of Mesozoic volcanic rocks in NE China: constraints on tectonic overprinting and transformations between multiple tectonic regimes. *Journal of Asian Earth Sciences* **74**, 167–93.
- Xu B, Zhao P, Wang YY, Liao W, Luo ZW, Bao QZ and Zhou YH (2015) The pre-Devonian tectonic framework of Xing'an-Mongolia orogenic belt (XMOB) in north China. *Journal of Asian Earth Sciences* **97**, 183–96.
- Yang W, Lin Y, Hao J, Zhang J, Hu S and Ni H (2016) Phosphorus-controlled trace element distribution in zircon revealed by NanoSIMS. *Contributions to Mineralogy and Petrology* **171**, 28. doi: [10.1007/s00410-016-1242-z](https://doi.org/10.1007/s00410-016-1242-z).
- Yogodzinski GM, Lees JM, Churkova TG, Dorendorf F, Wöerner G and Volynets ON (2001) Geochemical evidence for the melting of subducting oceanic lithosphere at plate edges. *Nature* **409**, 500–3.
- Yu Q, Ge WC, Yang H, Zhao GC, Zhang YL and Su L (2014) Petrogenesis of late Paleozoic volcanic rocks from the Daheshen Formation in central Jilin Province, NE China, and its tectonic implications: constraints from geochronology, geochemistry and Sr–Nd–Hf isotopes. *Lithos* **192–195**, 116–31.
- Yu JJ, Men LJ, Chen L, Zhao JK, Liang SN, Chen DP and Pang W (2008) SHRIMP U–Pb ages of zircon and its geological implications from metamorphic dacite of the Wudaogou group in Yanbian Area. *Journal of Jilin University (Earth Science Edition)* **38**, 363–7 (in Chinese with English abstract).
- Yuan L, Zhang X, Xue F, Lu Y and Zong K (2016) Late Permian high-Mg andesite and basalt association from northern Liaoning, North China: insights into the final closure of the Paleo-Asian ocean and the orogen-craton boundary. *Lithos* **258–259**, 58–76.
- Zack T, Tomascak PB, Rudnick RL, Dalpe C and McDonough WF (2003) Extremely light Li in orogenic eclogites: the role of isotope fractionation during dehydration in subducted oceanic crust. *Earth and Planetary Science Letters* **208**, 279–90.
- Zhang YB, Wu FY, Wilde SA, Zhai MG, Lu XP and Sun DY (2004) Zircon U–Pb ages and tectonic implications of 'Early Paleozoic' granitoids at Yanbian, Jilin Province, northeast China. *Island Arc* **13**, 484–505.
- Zhang SH, Zhao Y, Song B and Yang YH (2007) Zircon SHRIMP U–Pb and in-situ Lu–Hf isotope analyses of a tuff from western Beijing: evidence for missing Late Paleozoic arc volcano eruptions at the northern margin of the North China block. *Gondwana Research* **12**, 157–65.
- Zhang SH, Zhao Y, Ye H, Liu JM and Hu ZC (2014) Origin and evolution of the Bainaimiao arc belt: implications for crustal growth in the southern Central Asian Orogenic Belt. *Geological Society of America Bulletin* **126**, 1275–300.
- Zhou JB and Wilde SA (2013) The crustal accretion history and tectonic evolution of the NE China segment of the Central Asian Orogenic Belt. *Gondwana Research* **23**, 1365–77.